(2) LEVEL II

AFML-TR-79-4021

AD A072175

STRAIN RATE EFFECTS ON ULTIMATE STRAIN OF COPPER

D. P. Bauer
S. J. Bless
University of Dayton Research Institute
300 College Park Avenue
Dayton, Ohio 45469

May 1979

October 1976 - October 1977

Approved for public release; distribution unlimited.

AIR FORCE MATERIALS LABORATORY
AIR FORCE WRIGHT AERONAUTICAL LABORATORIES
AIR FORCE SYSTEMS COMMAND
WRIGHT-PATTERSON AIR FORCE BASE, OHIO 45433

79 08 1 071

NOTICE

When Government drawings, specifications, or other data are used for any purpose other than in connection with a definitely related Government procurement operation, the United States Government thereby incurs no responsibility nor any obligation whatsoever; and the fact that the government may have formulated, furnished, or in any way supplied the said drawings, specifications, or other data, is not to be regarded by implication or otherwise as in any manner licensing the holder or any other person or corporation, or conveying any rights or permission to manufacture, use, or sell any patented invention that may in any way be related thereto.

This report has been reviewed by the Information Office (OI) and is releasable to the National Technical Information Service (NTIS). At NTIS, it will be available to the general public, including foreign nations.

This technical report has been reviewed and is approved for publication.

THEODORE NICHOLAS, AFML/LLN
Project Engineer

NATHAN G. TUPPER, Chief
Metals Behavior Branch
Metals and Ceramics Division

If your address has changed, if you wish to be removed from our mailing list, or if the addressee is no longer employed by your organization, please notify AFML/LLN, W-PAFB, OH 45433 to help us maintain a current mailing list.

Copies of this report should not be returned unless return is required by security considerations, contractual obligations, or notice on a specific document.

UNCLASSIFIED

SECURITY CLASSIFICATION THIS PAGE (When Data Entered)

REPORT DOCUMENTATION PAGE

READ INSTRUCTIONS BEFORE COMPLETING FORM

1. REPORT NUMBER: AFML-TR-79-4021	2. GOVT ACCESSION NO.
3. RECIPIENT'S CATALOG NUMBER	
4. TITLE (and Subtitle): STRAIN RATE EFFECTS ON ULTIMATE STRAIN OF COPPER.	5. TYPE OF REPORT & PERIOD COVERED: Technical Report: Oct. 1976 — Oct. 1977
	6. PERFORMING ORG. REPORT NUMBER: UDR-TR-78-45
7. AUTHOR(s): D. P. Bauer, S. J. Bless	8. CONTRACT OR GRANT NUMBER(s): F33615-76-C-5124
9. PERFORMING ORGANIZATION NAME AND ADDRESS: University of Dayton Research Institute, 300 College Park Avenue, Dayton, OH 45469	10. PROGRAM ELEMENT, PROJECT, TASK AREA & WORK UNIT NUMBERS: 2307-P1-07
11. CONTROLLING OFFICE NAME AND ADDRESS: Air Force Materials Laboratory/LLN, Wright-Patterson Air Force Base, OH 45433	12. REPORT DATE: May 1979
	13. NUMBER OF PAGES: 77
14. MONITORING AGENCY NAME & ADDRESS (if different from Controlling Office)	15. SECURITY CLASS. (of this report): UNCLASSIFIED
	15a. DECLASSIFICATION DOWNGRADING SCHEDULE

16. DISTRIBUTION STATEMENT (of this Report)

Approved for Public Release; distribution unlimited.

17. DISTRIBUTION STATEMENT (of the abstract entered in Block 20, if different from Report)

18. SUPPLEMENTARY NOTES

19. KEY WORDS (Continue on reverse side if necessary and identify by block number)

Copper, Strain Rate, Ultimate Strain, High Rate

20. ABSTRACT (Continue on reverse side if necessary and identify by block number)

The strain-rate effect on strain to failure of copper was experimentally investigated. Both Oxygen Free High Conductivity (OFHC) copper and Electrolytic Tough Pitch (ETP) copper were studied. Ultimate strains were measured for a range of strain rates from 0.0001 strain/second to over 10000.0 strain/second. Normal quasi-static tensile machines were used at low strain rates, a split Hopkinson bar apparatus was used at strain rates of 1000.0 strain/second, and an exploding tube technique was developed

DD FORM 1 JAN 73 1473 EDITION OF 1 NOV 65 IS OBSOLETE

UNCLASSIFIED

SECURITY CLASSIFICATION OF THIS PAGE (When Data Entered)

105400

for strain rates to over 10000.0 strain/second. High speed photographic techniques and post shot fragment analysis were used to determine the strain rate effects.

Copper shows little strain rate dependence below 1000.0 strain/second with average ultimate strains around 0.4. Above approximately 5000.0 strain/second, several geometrical and material related factors cause the average ultimate strain to increase to values above 1.3, due to suppression of necking in the material until very late in the straining process. OFHC copper and ETP copper behave much the same to strain rates of 10000.0 strain/second.

FOREWORD

The program described in this report was carried out for the Air Force Materials Laboratory. The work was done under Contract F33615-76-C-5124. Dr. Theodore Nicholas was the monitor for that contract.

Mr. David Bauer served as Principal Investigator on the project. The experiments were conducted by Mr. Philip Kern. Dr. John Barber was responsible for overall technical supervision and Mr. Hallock Swift was Project Supervisor.

The authors wish to acknowledge the great help of Mrs. Sue Gainor during the preparation of this report.

TABLE OF CONTENTS

LIST OF ILLUSTRATIONS

LIST OF ILLUSTRATIONS (CONT'D)

LIST OF TABLES

SECTION I
INTRODUCTION AND SUMMARY

1.1 INTRODUCTION

In recent years analysis of physical events involving large deformation and flow of materials has become feasible with the advent of sophisticated computer codes. Many of the large deformation events of interest occur in very short time periods. The lack of good data on material properties at high strain rates has limited the accuracy of the results of computer assisted analyses. Material properties measured at quasi-static strain rates often change when high strain rates are applied. Work is now underway to generate this required high strain rate material properties data.

The subject of this report is the effect of strain rate on ultimate failure of copper. The objective of this study was to experimentally determine the strain to failure for copper at strain rates to greater than 1×10^4 strain per second (s^{-1}). Two types of copper, Electrolytic Tough Pitch (ETP) and Oxygen Free High Conductivity (OFHC) were studied.

Three separate experimental techniques were used to obtain strain rates in the range from $1 \times 10^{-4} s^{-1}$ to $4 \times 10^4 s^{-1}$. A closed-loop control hydraulic test machine was used to find ultimate strain at strain rates of $\sim 10^{-4} s^{-1}$ and $10^0\ s^{-1}$. A tensile split Hopkinson bar apparatus was used to obtain ultimate strain at strain rates near $10^3 s^{-1}$. An exploding cylinder technique was developed for strain rates to $4 \times 10^4 s^{-1}$.

Nearly constant average ultimate strains of approximately 0.40 were measured for strain rates from $10^{-4} s^{-1}$ to $10^3 s^{-1}$. Above $10^3 s^{-1}$ the average ultimate strain increased rapidly, to approximately 1.10 at a strain rate of $4 \times 10^4 s^{-1}$. Ultimate strain measurements were also made in the necked region of all

specimens tested. In general, as strain rate increased the necked region became less significant and straining was much more evenly distributed throughout the bulk of the material.

1.2 BACKGROUND

Few test procedures are available for tensile property determination at high strain rates. Conventional testing machines operate at $< 10\ s^{-1}$. In the last few years, several techniques have been developed for up to $10^3 s^{-1}$. Shock physics provides methods for studying the range of 10^5 to $10^6 s^{-1}$. However, until now there has been no satisfactory means to determine tensile properties in the critical neighborhood of $\sim 10^4 s^{-1}$. A brief review of high strain rate testing techniques is presented below.

Manjoine[1] conducted tensile tests using a hydraulic tension testing machine to determine the rate sensitivity of mild steel. The highest strain rates achieved were around $10^2 s^{-1}$ (typical of the maximum strain rates achievable with this method). The test results were seriously affected by wave propagation effects related to the dynamic elastic deformation of the machine itself.

The split Hopkinson bar tensile test was used by Nicholas[2] to obtain tensile strain rates up to $10^3 s^{-1}$ on Beryllium and several other materials. This technique provides direct measurements of stress and strain under uniaxial stress conditions. The technique could probably be extended to controlled triaxial stress states by employing notched tensile specimens as suggested by Hancock[3]. Hancock has used the notched tensile specimen in a hydraulic tension machine at quasi-static strain rates to investigate triaxial stress states in mild steel.

To obtain strain rates up to $10^3 s^{-1}$, Bitans[4] and Duffy[5] used high speed torsional testing machines. They obtained nearly constant rates of strain in thin-walled tubular specimens of copper, aluminum, and lead. Problems were encountered with

this technique, due to changes in the specimen geometry during the test and the low frequency response of the dynamometer system employed.

Several impact techniques have been used to produce higher tensile strain rates. Japanese investigators used explosively launched annular flyer plates to produce uniaxial tensile stress in austenitic stainless steel.[6] This technique is limited because the strain rate is a strong function of strain. Shultz[7,8] has attained strain rates between 10^2 and $10^3 s^{-1}$ with transverse impacts onto thin wires. The study of plasticity is difficult with this technique because the analysis is based on propagating elastic waves. The strain rate is not constant during the test, and the maximum strain rate achievable is limited by the severing velocity of the wire.

Expanding ring tests have been done at strain rates up to $0.8 \times 10^4 s^{-1}$ by Hoggatt et. al.[9] A 50-mm-diameter specimen ring was fitted onto a massive steel driving cylinder which contained an axial explosive filled chamber. Detonation of the explosive produced radial shock waves in the cylinder, which caused the ring to spall off. The ring expanded due to the radial momentum and tensile hoop stresses were generated in the ring. The other two principal stresses were nominally zero. These investigators observed maximum strains of only 12 percent in mild steel, aluminum, and titanium. The strain rate varied during the experiment due to deceleration of the ring. The maximum energy transfer to the ring (radial velocity) was insufficient to induce failure in ductile specimens.

SECTION II
EXPERIMENTAL PROCEDURES

This section describes the experimental techniques which were employed to determine the ultimate strain of copper at strain rates from $10^{-4}s^{-1}$ to above $10^{4}s^{-1}$.

2.1 INTRODUCTION

Three techniques were used to determine the ultimate strain of ETP copper and OFHC copper at various strain rates. Each testing method was used over a specific range of strain rates. The three techniques included a conventional hydraulic materials testing machine for strain rates of $10^{-4}s^{-1}$ and $1\ s^{-1}$, a split Hopkinson bar apparatus for strain rates up to $10^{3}s^{-1}$, and an explosively expanded cylinder technique for strain rates exceeding $10^{4}s^{-1}$. These techniques were selected to produce essentially uniaxial tensile stress-strain conditions in the respective specimens.

The hydraulic testing machine and Hopkinson bar specimens were the usual "dogbone" shaped tensile specimen. The exploding cylinder test employed a right circular tubular specimen with length to diameter ratio of 8:1.

Two types of copper were studied in these experiments, Electrolytic Tough Pitch (ETP 110, ASTM designation B187) and Oxygen Free High Conductivity (OFHC, ASTM designation B75 (OF)). All specimens were fully annealed prior to testing.

2.2 QUASI-STATIC TEST SETUP

At the lower strain rates ($10^{-4}s^{-1}$ to $1\ s^{-1}$) a closed loop electro-hydraulic machine was used to load the specimens. Loads were measured with the load cell in the machine, and a

differential transformer type extensometer was attached across the specimen to monitor strain. Strain was also measured by manually monitoring the diameter of the specimen during straining. When necking occurred the diameter measurements were made in the necked region of the specimen, and the ultimate strain determinations were based on these measurements (as will be discussed later). A uniform nominal strain rate was maintained with a strain rate pacer. The specimens for this test were machined from solid drawn round stock of ETP copper. The usual "dogbone" shape with dimensions as shown in Figure 1 was employed. The machining was done such that longitudinal axes of the specimen and stock coincided. After machining, the specimens were annealed at 538°C for one hour in a vacuum.

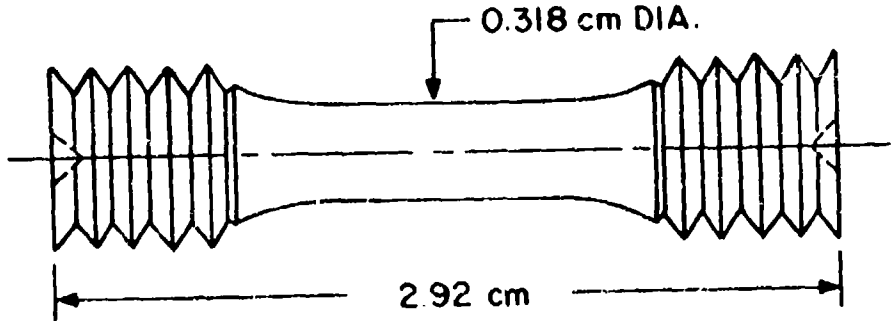

Figure 1. "Dogbone" Specimen Used for Quasi-Static and Intermediate Strain Rate Tests

2.3 SPLIT HOPKINSON BAR TEST SETUP

The tension tests at the intermediate strain rates (i.e., $10^3 s^{-1}$) were performed on a split Hopkinson bar apparatus developed at the Air Force Materials Laboratory and described in Reference 2. The device is shown schematically in Figure 2. This split Hopkinson bar apparatus is capable of testing materials in tension at maximum strain rates of about $10^3 s^{-1}$. The apparatus consists of three main parts; a striker bar, and two Hopkinson pressure bars. When impacted by the striker, an elastic compression wave travels down the incident bar through the shoulder and into the transmitter bar as shown in Figure 2. The compression wave is reflected at the far end of the transmitter bar as a tensile wave. When this tensile wave reaches the test specimen, elongation of the specimen begins, since the shoulder interface cannot support tensile stresses. The "dogbone" specimen illustrated in Figure 1 was used. Data are in the form of load versus cross-head displacement and are obtained from the strain gauges attached to the pressure bars. Strain is calculated from an empirical formula relating head displacement to strain and gauge length, obtained using strain gauges on dummy calibration specimens. The calculated strain, assumed uniform along the gauge length, does not take into account necking if it occurs. Independent measurements to determine true ultimate strain of the failed specimen were made. The derivation of the equation for true strain obtained with this measurement may be found later in this section. The strain rate in these experiments was calculated as the time derivative of the strain measured during the experiment. This strain rate is negligibly different from the true strain rate as described later. True stress was calculated from load divided by actual area (original area corrected due to uniform axial strain, assuming incompressible plastic flow). The specimens for this test were machined from the same piece of round bar stock and with the same directionality as that used

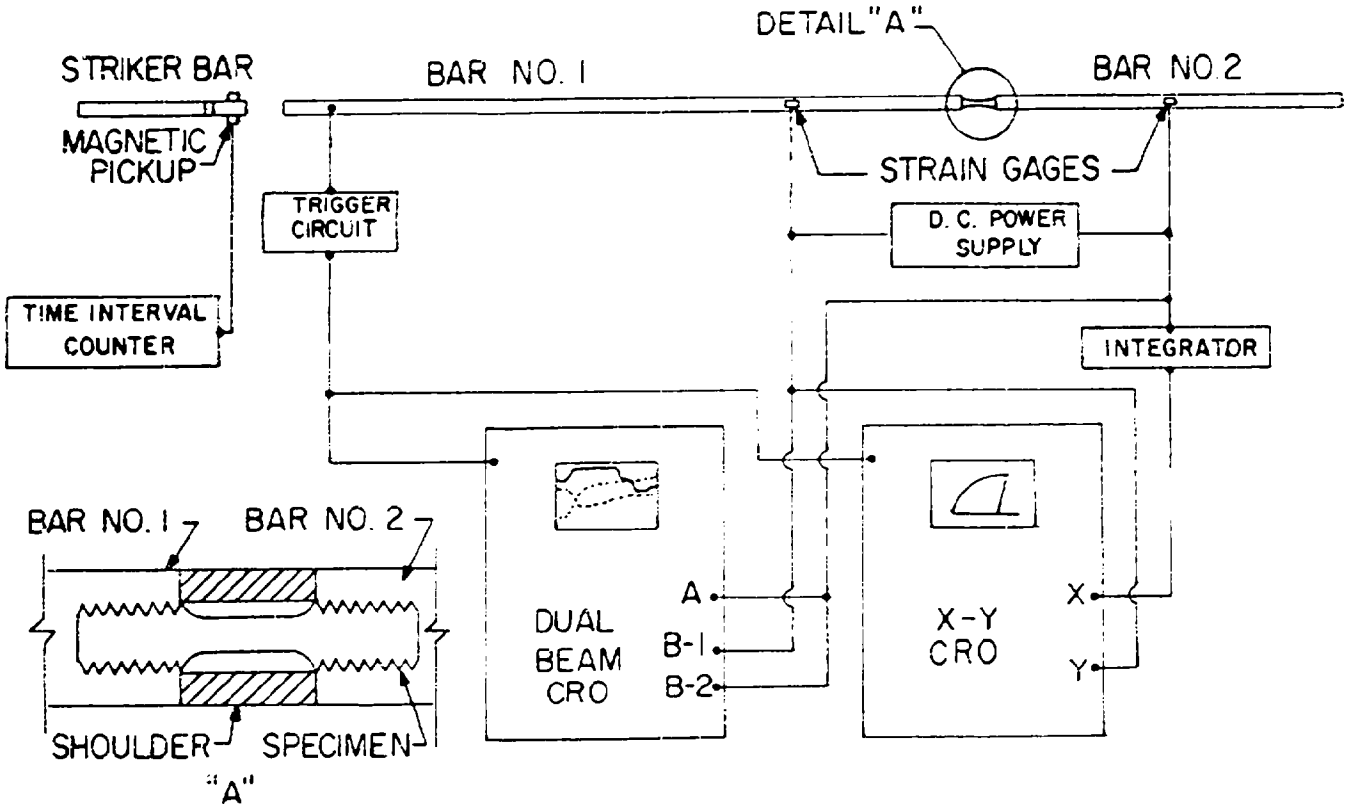

Figure 2. Schematic of Split Hopkinson Bar Apparatus

for the quasi-static test specimens. The specimens were annealed in a vacuum at 538°C for one hour.

2.4 EXPANDING TUBES

The technique developed for the evaluation of ultimate strain at strain rates above $10^4 s^{-1}$ employed explosively expanded cylindrical tubes. When detonated the explosive pressures produced radial motion of the material. Tensile hoop stresses were generated in the tube during expansion to failure.

The ETP tubes were 152 mm long, with an outside diameter of 19 mm, and a wall thickness of 1.92 mm. The ETP tubes were manufactured by boring and honing a hole in drawn solid round stock. The stock material was part of the same bar from which the "dogbone" specimens were made. This procedure produced a good surface finish with circumferential machining artifacts on the tube.

Due to material availability problems, sizes and manufacturing techniques for the OFHC tubes were not constant. Some were specimens made by sectioning OFHC drawn tubing. The other fabricating technique was similar to that used for the ETP specimens. The drawing operation left small longitudinal mars on the tube. These imperfections were reduced by hand honing the tubes. Once these manufacturing operations were completed, the tubes were annealed at 538°C for one hour in a vacuum, then furnace cooled to room temperature. This annealing process resulted in a material hardness of 41 R_F (Rockwell "F" scale uses 1/16" diameter indenter with a 60 KG load). This hardness corresponds to a 0.050-mm temper as specified by the American Society for Metals.[10]

Two types of explosive loadings were used in the tube geometry, as shown in Figure 3a and 3b. Each loading provided a different strain rate at failure. For the highest strain rates, pentaerythritoltetranitrate (PETN) filled cylinders

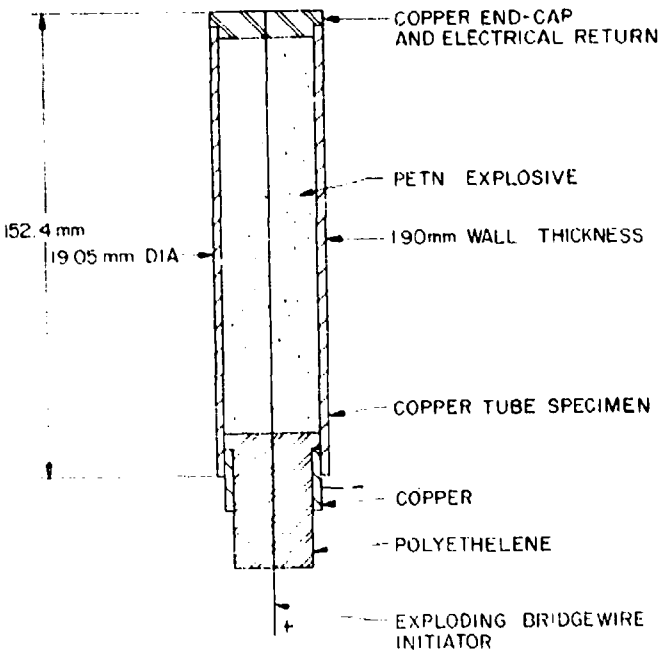

Figure 3a. PETN Filled Tube Specimen Detonated by Exploding Bridgewire Specimen

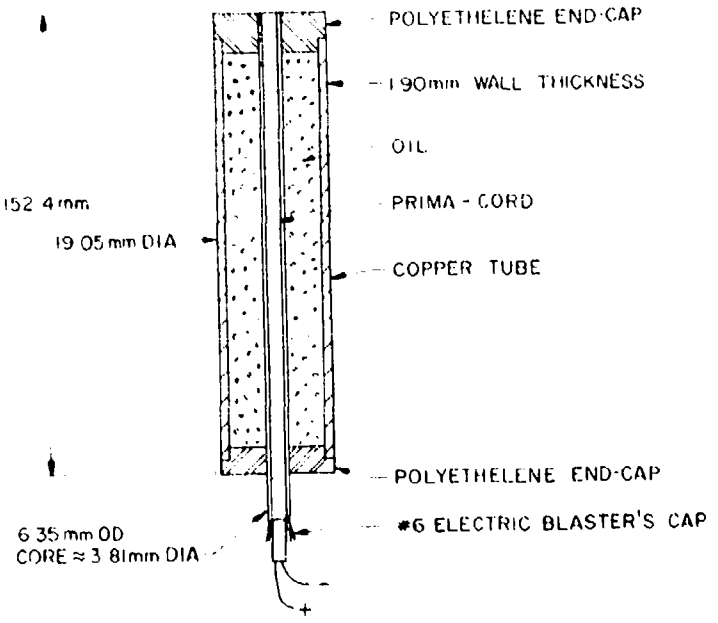

Figure 3b. Prima-Cord Tube Specimen Detontated by Electric Blaster's Cap

were used. These tubes were loaded incrementally with HE by pressing 2.02 gram quantities of PETN individually into the tube. Each of 12 pressings needed to fill the tube was individually compressed, to obtain an average density of 0.88 g/cm^3. This method resulted in a more uniform packing density than could otherwise be obtained through one pressing of the total volume of material.

At 0.88 g/cm^3 packing density, PETN is most sensitive to detonation by the exploding bridgewire technique.[11] The wire used in these experiments was 0.127-mm-diameter platinum. By discharging the stored energy in a low inductance capacitor bank into the wire, simultaneous initiation of the explosive was expected to provide uniform expansion of the tube. Due to local end effects of the exploding bridgewire, however, initiation of the explosive occurred somewhat sooner at the tube end than elsewhere.

For the lower strain rates ($1 \times 10^4 s^{-1}$), a length of Prima-Cord was coaxially positioned in the tube with the remaining volume being filled with hydraulic-type oil. The Prima-Cord had a 2.5-mm-diameter core of explosive, and detonation was initiated with an electric blasting cap attached at one end.

2.5 LAWRENCE LIVERMORE LABORATORY (LLL) EXPERIMENTS

Kury, et al,[12] at Lawrence Livermore Laboratories have explosively expanded metallic cylinders for many years. Their objective in the experiments was to investigate the relative metal-accelerating ability of various explosives. They did not study the strain rate ultimate strain properties of the metals used in those studies.

In the LLL experiments OFHC copper tubes of various sizes (30 mm to 100 mm ID) were expanded explosively, using many types of explosives. All of the experiments used electric blasting caps attached at one end for explosive initiation. This technique caused the circular cylindrical tubes to expand with

a conical shape. Simultaneous framing camera and streak camera records were obtained. UDRI and LLL conducted a technical interchange in which their data were examined. Due to the experimental technique used by them, only a small fraction of their data were useful for calculating ultimate strain.

2.6 RANGE DESCRIPTION FOR UDRI EXPLODING CYLINDER TESTS

A photograph of the indoor range used to conduct the expanding tube tests at UDRI is shown in Figure 4. This range is physically located in a separate building, originally designed for shock tube work, on the University campus. The building has two rooms, one of which contains the range (Figure 4) and the other contains the control equipment (not shown).

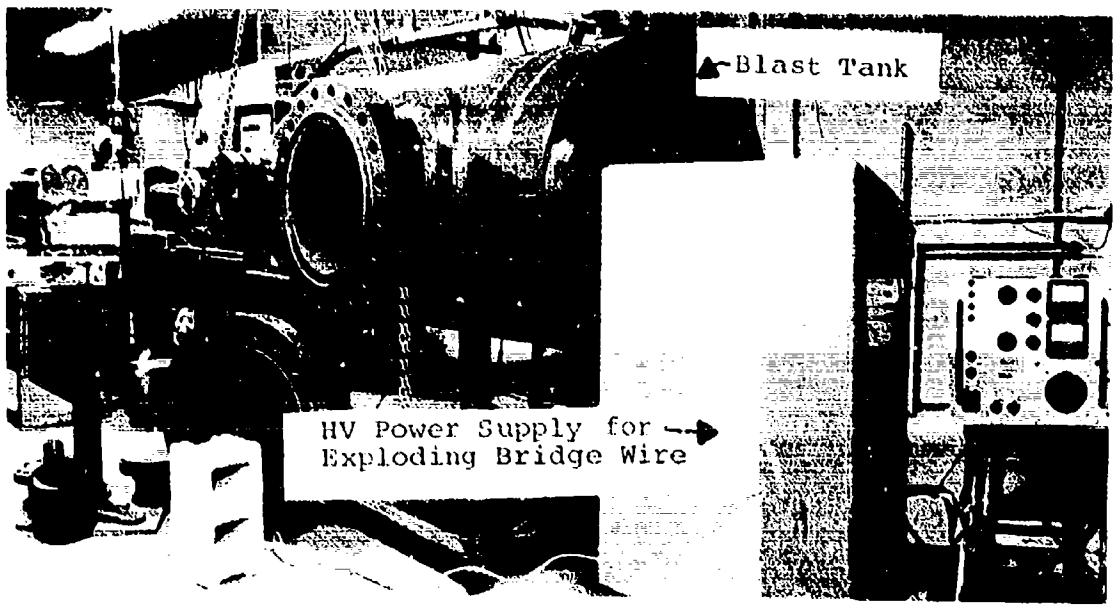

Figure 4. UDRI Range for Exploding Tube Tests

The blast tank used to contain the explosive debris in these experiments is part of a multiuse range. This steel tank is 90 cm inside diameter by 150 cm long, with a wall thickness of 3 cm. The tank ends are elliptical to provide higher pressure capabilities (~500 g of HE). The tank is equipped with a 46-cm diameter man access port, two 23-cm diameter ports for optical access, and several smaller ports used for vacuum system connection and electrical cable feedthrough.

All tube experiments were conducted at room temperature (~20°C) and in an air atmosphere at 125 mm of mercury. This partial vacuum reduced degradation of the photographic records by air shocks.

The exploding tubes were mounted in the blast tank on a large permanently attached I-beam. This mounting base allowed a rigid attachment of the tube to be made and provided ease of locating the tube in the optical field of view. A typical mounting is shown in Figure 5. In the design of this mount, care was taken to prevent external clamping on the ends of the tube (see Figure 3), thus reducing end effects on the deformation of the tube as much as possible.

The exploding bridgewire circuit was designed for low inductance operation so that the stored energy of the capacitor bank could be transferred to the bridgewire more efficiently. Three capacitors of 0.04 μH inductance each were connected in parallel, for a total capacitance of 38.4 μF. These capacitors were charged to 19.5 KV for the experiments. The stored energy was switched to the bridgewire using a spark gap switch. A pair of parallel low inductance coaxial cables carried the energy to the bridgewire. This cable has an inductance of 33 nH/ft. The total inductance of the exploding bridgewire circuit was 0.4 μH.

A Beckman and Whitley Model 300 rotating mirror continuous access framing camera was utilized to photograph the tube expansion. This camera has a 48 frame format with framing

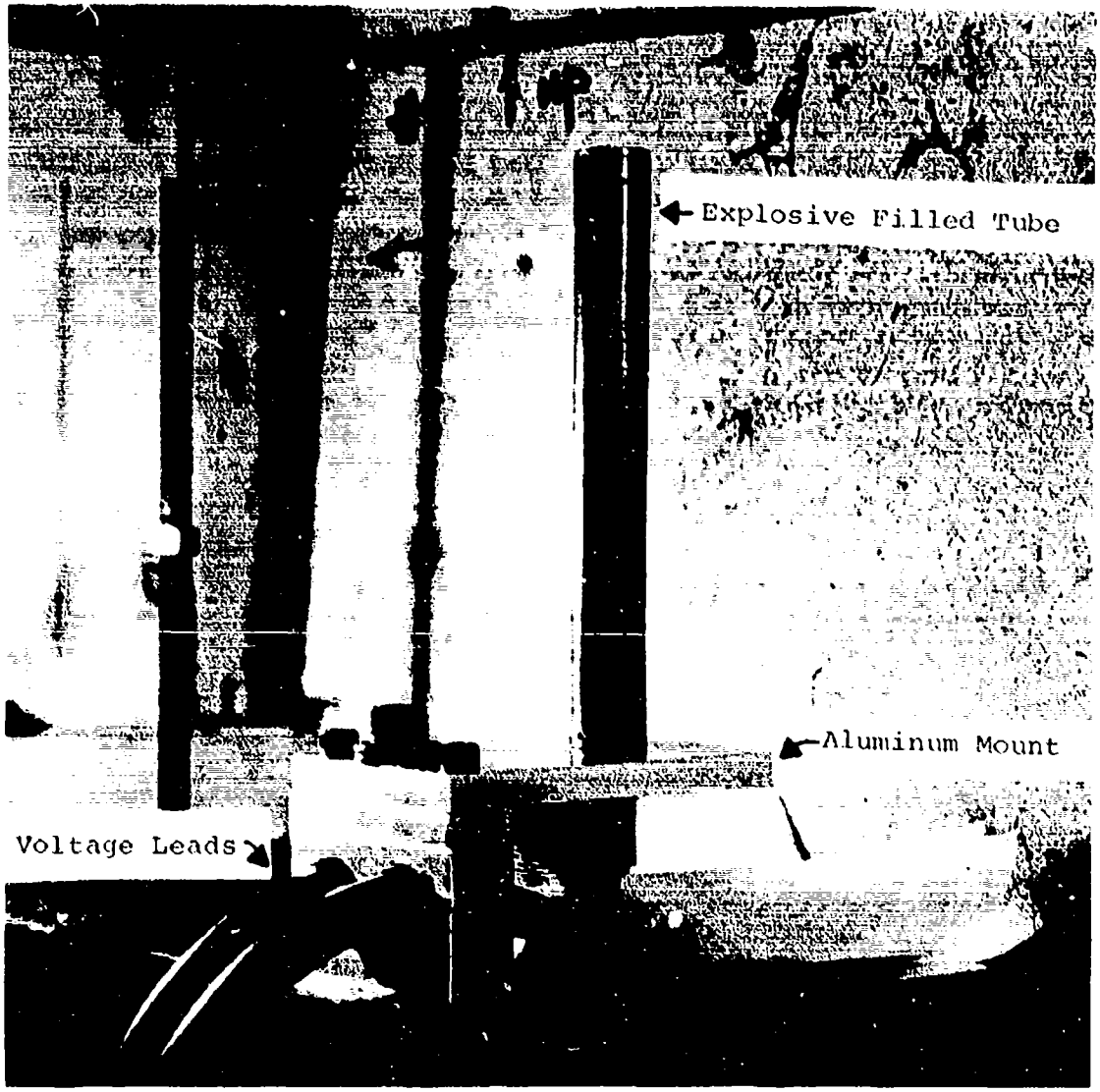

Figure 5. Typical Mount of Explosive Tube in Blast Tank

rates up to 4.5×10^{-6} f/s. For these cylinder tests the camera was operated at $\sim 1 \times 10^{6}$ f/s. Interframe corrections of Preonas[13] were used for reducing data of the framing camera records. A schematic of the optical setup for the tests is shown in Figure 6. As may be seen, the tube was back-lit. The illumination was provided with a spark-gap light source and a twin-element 255-mm-diameter condenser lens. The gap was energized with a 30 μF, 18 KV capacitor bank. The light source provided sufficient light for recording, with a duration of ~55 μs. The triggering pulse to the light source was delayed 10 μs behind the triggering pulse to the exploding bridgewire capacitor bank. This provided time for detonation to begin, so that failure could be detected on the framing camera record.

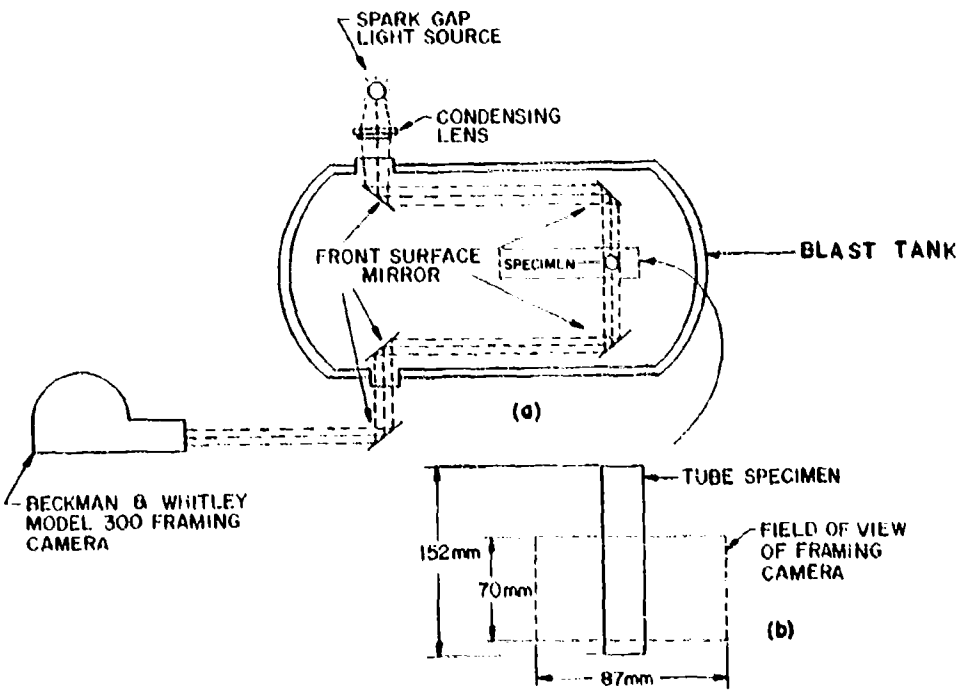

Figure 6. Optical Setup for Monitoring Exploding Tube Event Inside of Blast Tank

2.7 THEORETICAL DERIVATION OF STRAIN

2.7.1 Strain Measurement in Tensile Specimens

For the "dogbone" specimens used in the static tests and the split Hopkinson bar tests (Figure 1), the true strain based on diameter measurements is derived as below.

Increments of true strain are defined as dL/L where L is the actual gauge length at any moment and dL is the incremental change in length caused by an incremental increase in load. The true strain ε at any load is found from:

$$\varepsilon = \int_{L_o}^{L} dL/L = \log_e L_f/L_o$$

Assuming that the volume remains constant during straining, then:

$$V_o = A_o L_o = V_f = A_f L_f$$

where V_o, A_o, and L_o are the volume, cross-sectional area and the gauge length respectively, before a load is applied. V_f, A_f, and L_f are the same respective values under load f. Then:

$$\frac{A_o}{A_f} = \frac{L_f}{L_o}$$

and

$$\varepsilon = \log_e \frac{A_o}{A_f}$$

The area is related to the diameter by:

$$A = \frac{\pi}{4} (d^2)$$

so that the true strain may be found from:

$$\varepsilon = \log_e \frac{d_o^2}{d_f^2} \qquad (1)$$

where d_o is the original diameter and d_f is the final diameter.

2.7.2 Expanding Tube Strain, Strain Rate Derivation

The geometry of the expanding tube is shown in Figure 7. The derivation of strain for this geometry follows. In polar coordinates, the tangential strain displacement relation is given by:

$$\varepsilon_\theta = \frac{u}{r}$$

where u is the radial displacement at the radius r. This equation is valid for small values of strain (i.e., $\varepsilon \ll 1$) and is generally referred to as engineering or apparent strain. The so-called true or logarithmic strain is obtained by considering that the radial displacement u is actually Δr. For small u, $\Delta r \approx dr$ and the true strain would be obtained by summing all the Δr's due to an incrementally increased load from zero to f, or:

$$\varepsilon_\theta = \int_{r_o}^{r_f} \frac{dr}{r}$$

$$\varepsilon_\theta = \ln \frac{r_f}{r_o} \qquad (2)$$

To obtain tangential surface strain from the high speed framing camera records, only the outside radius need be measured.

The strain rate may be obtained by taking the derivative with respect to time of the strain. The result is given by:

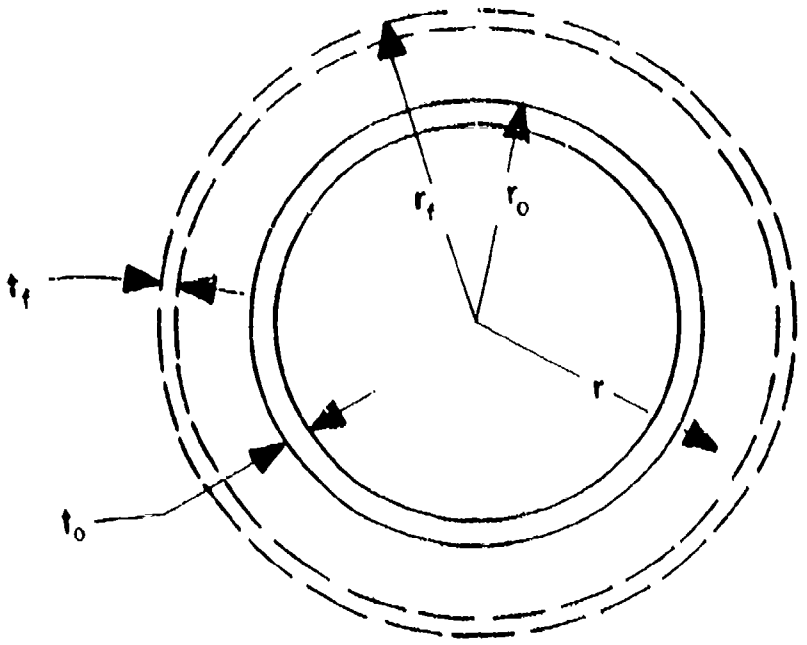

Figure 7. Geometry for Tube Strain Displacement Equations

$$\dot{\varepsilon} = \frac{\dot{r}}{r}$$

where $\dot{r}$ is the tube wall velocity at radius r.

These equations were used to reduce the photographic data from all the experiments.

2.7.3. Strain from Thickness Measurements

Strain in an expanding cylinder may also be obtained using wall thickness measurements if constant volume uniform deformation is assumed. This gives:

$$A_o \ell_o = A_f \ell_f$$

where ℓ refers to the tube length and the subscript f is the quantity at failure; the cross sectional area A, is given by:

$$A = 2\pi \bar{r} t$$

where $\bar{r}$ is the mean tube radius and t is the wall thickness. With the strain given by Equation 2:

$$\varepsilon = \ln \frac{r_f}{r_o}$$

and substituting from above the strain may be written as:

$$\varepsilon = \ln \frac{t_o \ell_o}{t_f \ell_f} \tag{3}$$

Implied in this derivation is the assumption that the tangential strain is uniform across the thickness of the tube. This assumption will be valid as long as $t/2r < 0.1$.

Assuming the tube length does not change during the expansion, Equation (3) becomes

$$\varepsilon = \frac{t_o}{t_f} \tag{4}$$

The validity of this assumption is checked in the Results section.

Use of Equation (4) to calculate strain in a necked region and in locations away from the neck will be analogous to using the diameter measurements of the tensile specimens in similar locations.

2.7.4. Radial Strain

In polar coordinates, the radial strain displacement relationship is given by

$$\varepsilon = \frac{\partial u}{\partial r}$$

which is also only valid for $\varepsilon_r << 1$, since the nonlinear terms have been dropped. This equation, as well as the equation for tangential strain, is based on assumptions that (1) the tube

expands symmetrically; and (2) that axial elongations are negligible. The validity of these assumptions will be checked in the section on Results. With these assumptions, the derivation will follow, as before, to give

$$\varepsilon_r = \ln \frac{t_f}{t_o}$$

The values given by this equation will be equal in magnitude, but opposite in sign of ε_θ.

SECTION II
EXPERIMENTAL RESULTS

3.1 MTS AND HOPKINSON BAR TESTS

A failed tensile specimen typical of those in the quasi-static tensile and Hopkinson bar experiments is shown in Figure 8. Table 1 is a summary of the data from these experiments. The strain rate data were calculated by differentiating the strain gauge output with respect to time, as discussed in Section II and in Reference 2. The strain data were derived from diameter measurements on the failed specimens. The values of average strain were calculated from the average diameter far from the necked region (i.e., greater than two diameters from fracture surface). Within the measurement uncertainty ($\sim$0.012 mm) the failed specimens were circular in cross section. Strains in the necked region were calculated from the diameter measurements with cross-sectional circularity uniform within $\sim$0.012 mm measurement accuracy. This indicates that the assumption of axial symmetry is valid.

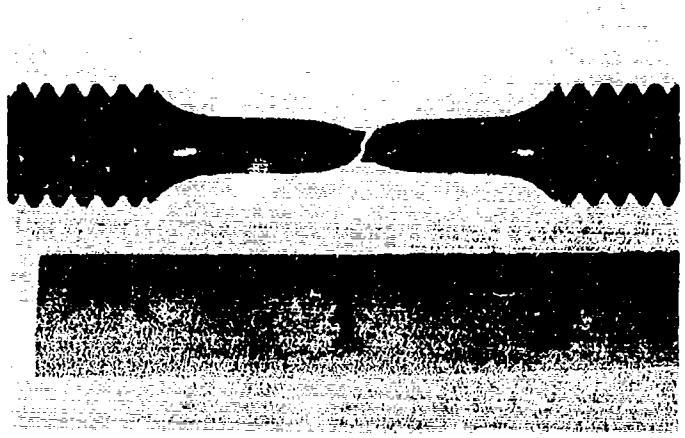

Figure 8. Typical Failed Low Strain Rate Specimen

TABLE 1

TENSILE SPECIMEN RESULTS

Strain Rate $\dot{\varepsilon}$ (s^{-1})	Original Diameter d_o (mm)	Average Final Diameter † d_f (mm)	Necked Final Diameter †† d_f (mm)	Average Strain $\bar{\varepsilon}_f$	Necked Strain ε_f
4.4×10^{-4}	3.20	2.66	1.46	0.37	1.57
4.4×10^{-4}	3.20	2.65	1.46	0.38	1.57
4.4×10^{0}	3.19	2.61	1.46	0.40	1.56
9.3×10^{2}	3.20	2.61	1.90	0.41	1.04
9.6×10^{2}	3.19	2.59	1.70	0.42	1.26
1.2×10^{3}	3.19	2.59	----	0.42	----
1.3×10^{3}	3.19	2.64	1.91	0.38	1.03

†Average diameter based on measurements of the uniformly strained region of the specimen.

††Final diameter based on measurements of the necked region of the specimen.

All diameter measurements were made by using the micrometer attachment on a magnifying optical comparator. (measurement accuracy = ±0.012 mm).

3.2 LAWRENCE LIVERMORE LABORATORY (LLL) DATA

A summary of the data obtained from the Lawrence Livermore Laboratory is shown in Table 2. A variety of explosives were used in several sizes of cylinders made of Oxygen Free High Conductivity, fully annealed copper. Back-lit streak and front-lit framing camera records were available from most of the LLL experiments. However, only a small fraction of these contained information on ultimate cylinder failure. Except where noted, the data reported here were reduced from streak camera records which provide better timing accuracy than the framing camera. The slits were positioned across the cylinders so that the slope on the streak record could be related to expansion velocity. Material failure was identified with a small change in slope which was usually followed by a loss of sharpness of the streak record. A schematic representation of a typical streak record is shown in Figure 9. Shown in Figure 10 are several frames of a typical cylinder from the LLL experiments. A comparison of measurements from the streak records and the framing records showed good agreement. However, the framing camera records showed highly localized premature material failure for shots 411 and 412. These localized failures were only conspicuous in the streak record data by the low ultimate strains attained when these failures occurred. Failures of this type were associated with high tube radius to wall thickness ratios, and also with the type of explosive being used. Some of the explosives such as RDX11 are relatively inhomogeneous, resulting in local "hot spots" in which localized pressure and temperature extremes occur. Combined with the low wall thickness, these "hot spots" cause tube failure very early in the expansion process by generating stress and strain concentration regions. The more homogeneous explosives, such as Nitromethane, usually resulted in uniform expansion. However, a number of shots with high r/t ratios showed premature failure. In the LLL tests, no fragment recovery attempts were made; thus, we were unable to study failure mechanisms for these experiments.

TABLE 2

SUMMARY OF STRAIN, STRAIN RATE FAILURE DATA DERIVED FROM END-DETONATED LIVERMORE CYLINDER TESTS

Shot Number	Explosive & Condition	Original Outer Tube Radius (f) R_o (mm)	Wall Thickness t (mm)	R_o/t	Radius at Failure R_f (mm)	Wall Velocity at Failure v_f (mm/μsec)	Tangential Strain at Failure (a), (e) ϵ_f	Strain Rate at Failure (b) $\dot{\epsilon}_f$ (1/sec)
392	Nitromethane	30.61	5.61	5.9	120.67	1.38	1.38 ± .10	1.15×10^4
293	9404	15.38	2.60	5.9	60.19	1.89	1.36 ± .05	3.14×10^4
410	LX072 Hollow Charge	25.13	1.00	25.1	68.89	1.97	1.01 ± .10	2.90×10^4
411(c)	RX11 BD Hollow Charge	50.29	2.00	25.1	88.43	1.57	.56 ± .10	1.76×10^4
412(c)	RX11 BD Hollow Charge	50.27	1.00	50.3	77.17	1.24	.43 ± .15	1.61×10^4
266	Nitromethane	14.08	1.30	10.8	48.96	1.80	1.25 ± .10	3.7×10^4

(a) $\epsilon = \ln \frac{R}{R_o}$

(b) $\dot{\epsilon} = \frac{v}{R}$

(c) Framing camera records show localized premature failure.

(d) Data from framing camera record.

(e) Uncertainty based on original data.

(f) All tubes made of OFHC copper.

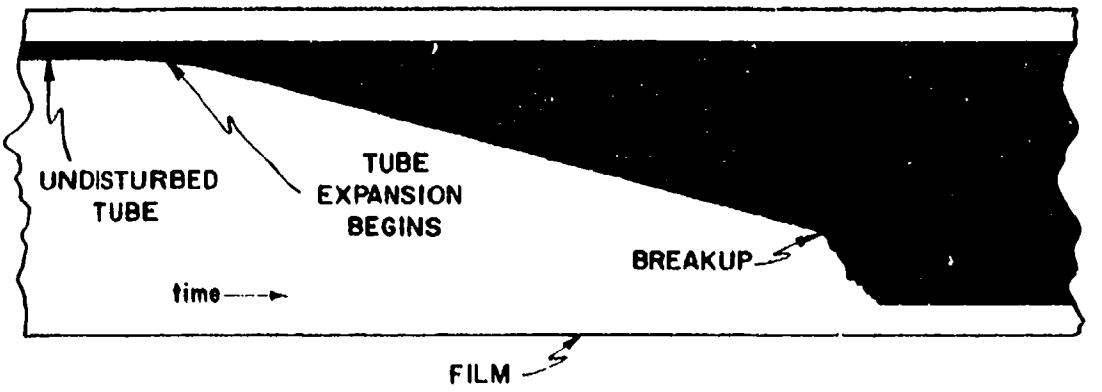

Figure 9. Schematic Representation of Expanding Cylinder on Streak Record

3.3 UDRI EXPLODING TUBE RESULTS

In the initial conception of the exploding cylinder plan, the failure radius was to be determined by the appearance of the explosive gases and detonation light through the opening cracks in the wall of the cylinder. This phenomena was not apparent on any of the UDRI records.

A typical framing camera record of a UDRI exploding tube event is shown in Figure 11. Fluctuations in onset and duration of the detonation process caused some difficulty in synchronizing the spark gap light source with the expansion of the cylinder. However, all film records did record tube failure. Failure was identified with the sudden appearance of jaggedness in the tube profile.

For several shots, radius measurements were made at more than one position along the cylinder length. This procedure was carried out for each frame on the record and for nonuniform expansions. For example, in Figure 11, the diameter was

(a) Begin expansion

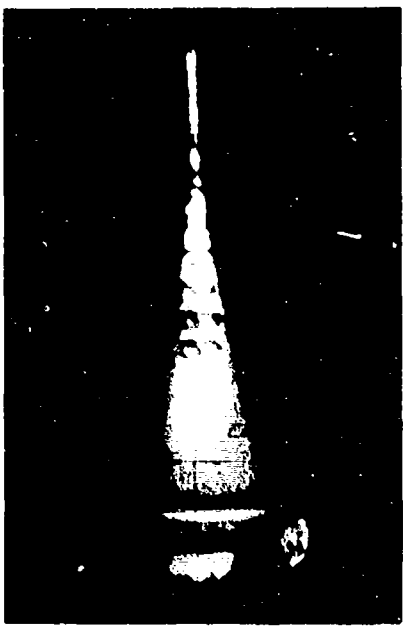

(b) Intermediate expansion

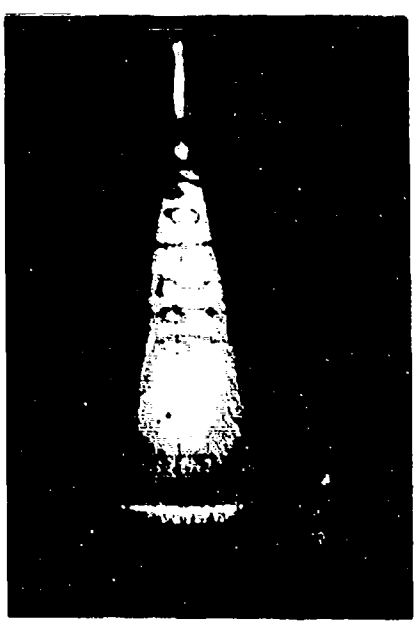

(c) Cracks form

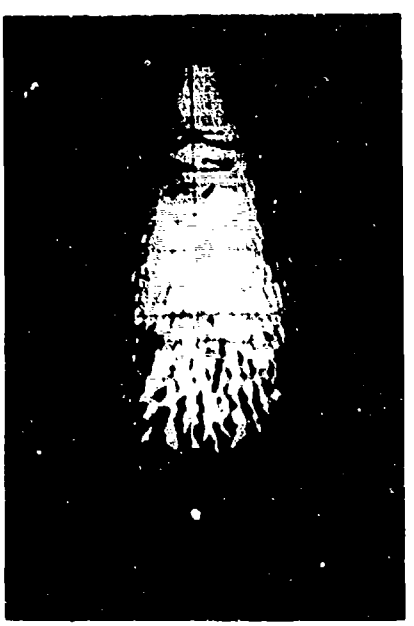

(d) Fracture

Figure 10. Expansion Process of LLL End-Detonated Cylinder

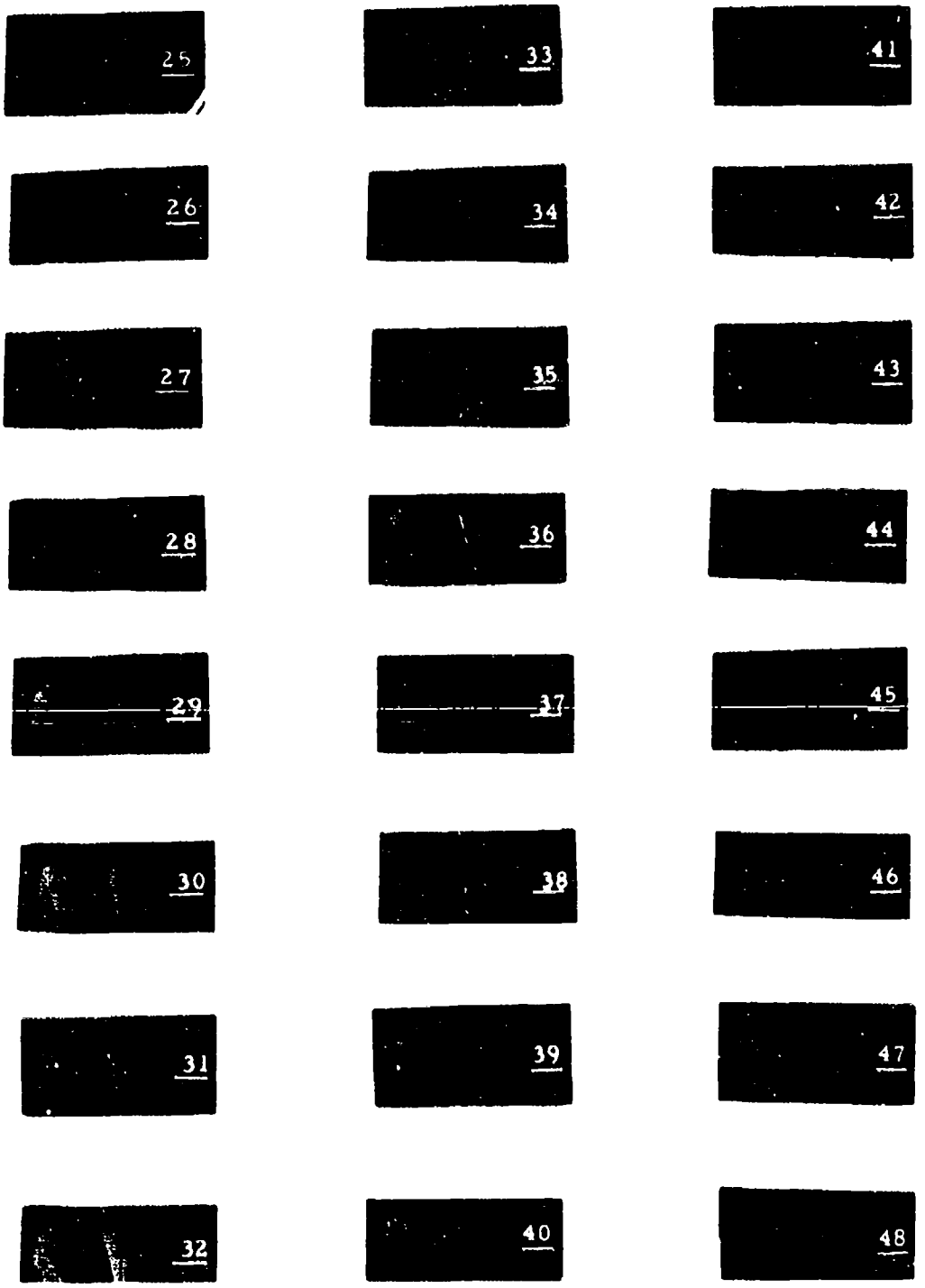

Figure 11a. Typical Camera Record of UDRI Expanding Tube Process (Right Side)

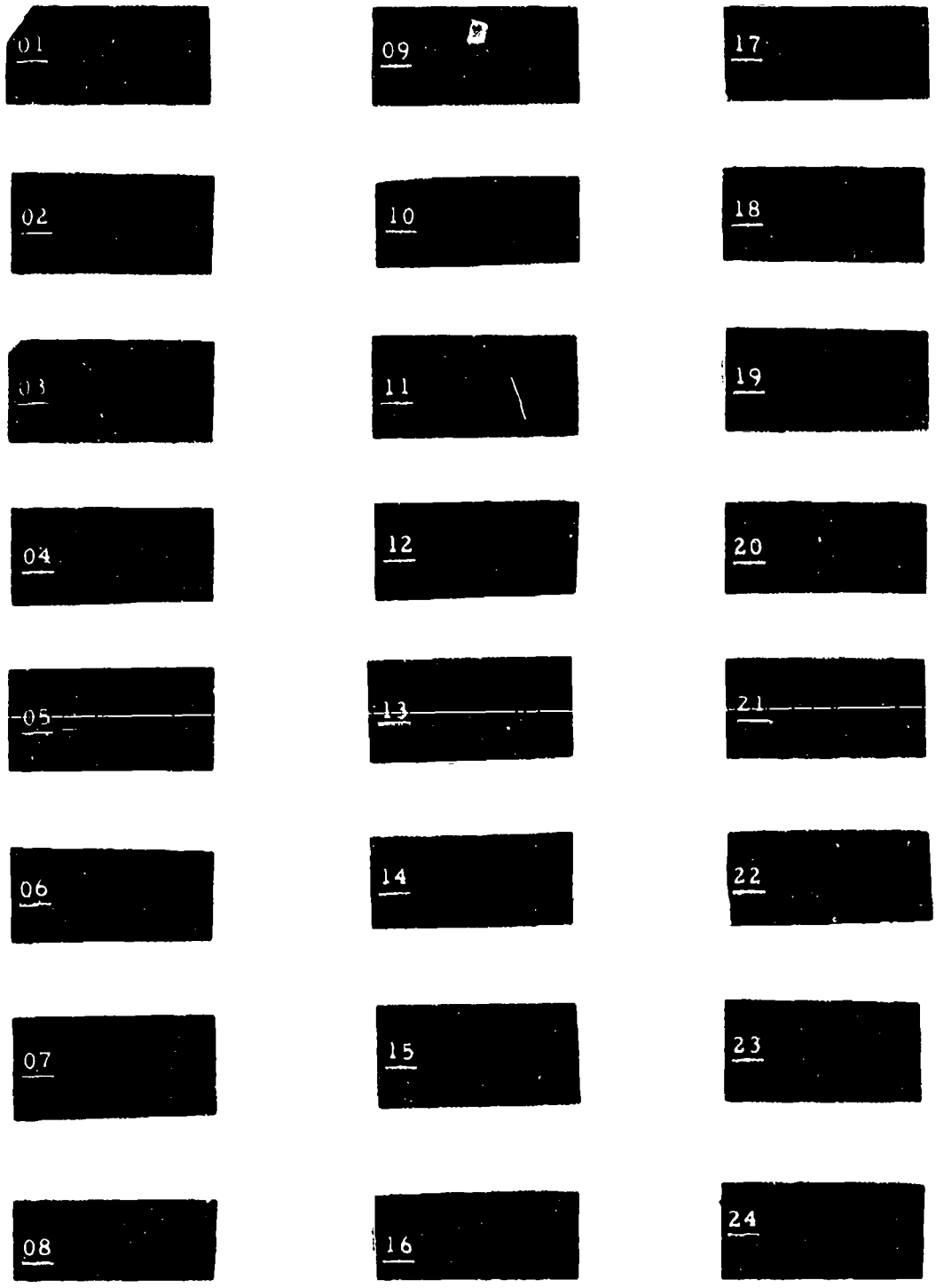

Figure 11b. Typical Framing Camera Record of UDRI Expanding Tube Process (Left Side)

measured at two locations along the length of the tube. The data from these measurements were then plotted as shown in Figure 12. (Other strain versus time plots are shown in Appendix A, along with the framing camera records.) For the measured shots, failure radius was found to depend slightly on axial position z. In Figure 12, for example, the ultimate strain indicated at midlength is $\sim$8 percent lower than at the position one-quarter length from one end. Thus, the ultimate strain at the higher strain rates (i.e., $>1 \times 10^4 s^{-1}$) for these tests is probably slightly less than that which would occur in true uniform expansion test. Unfortunately, the correction may not be quantitatively established from the present results.

Recovered fragments from an exploding cylinder experiment are shown in Figure 13. The ultimate strain measured from the framing camera record was checked by making thickness measurements on collected tube fragments. The results of these measurements are shown in Table 3. Two sets of thickness measurements appear in this table. The average thickness measurements were made at locations on the fragments more than two thicknesses away from any fractured edge. This thickness measurement therefore does not take into account necking which occurred in the specimen near the fracture surface. The other thickness measurements, a direct measurement of the necking, was made at distances not greater than one thickness away from the failure surface. This is a measurement of the minimum thickness which occurred in the necked region. These thicknesses are actually an average of several measurements made on numerous tube fragments. The uncertainty attached to the average thicknesses is the standard deviation of the measurements.

A relatively large number (i.e., greater than 20) of these thickness measurements were made on the specimens. Good uniformity (to within measurement error) of these thicknesses over the many pieces measured indicates that at any cross section uniform expansion of the tubes was obtained.

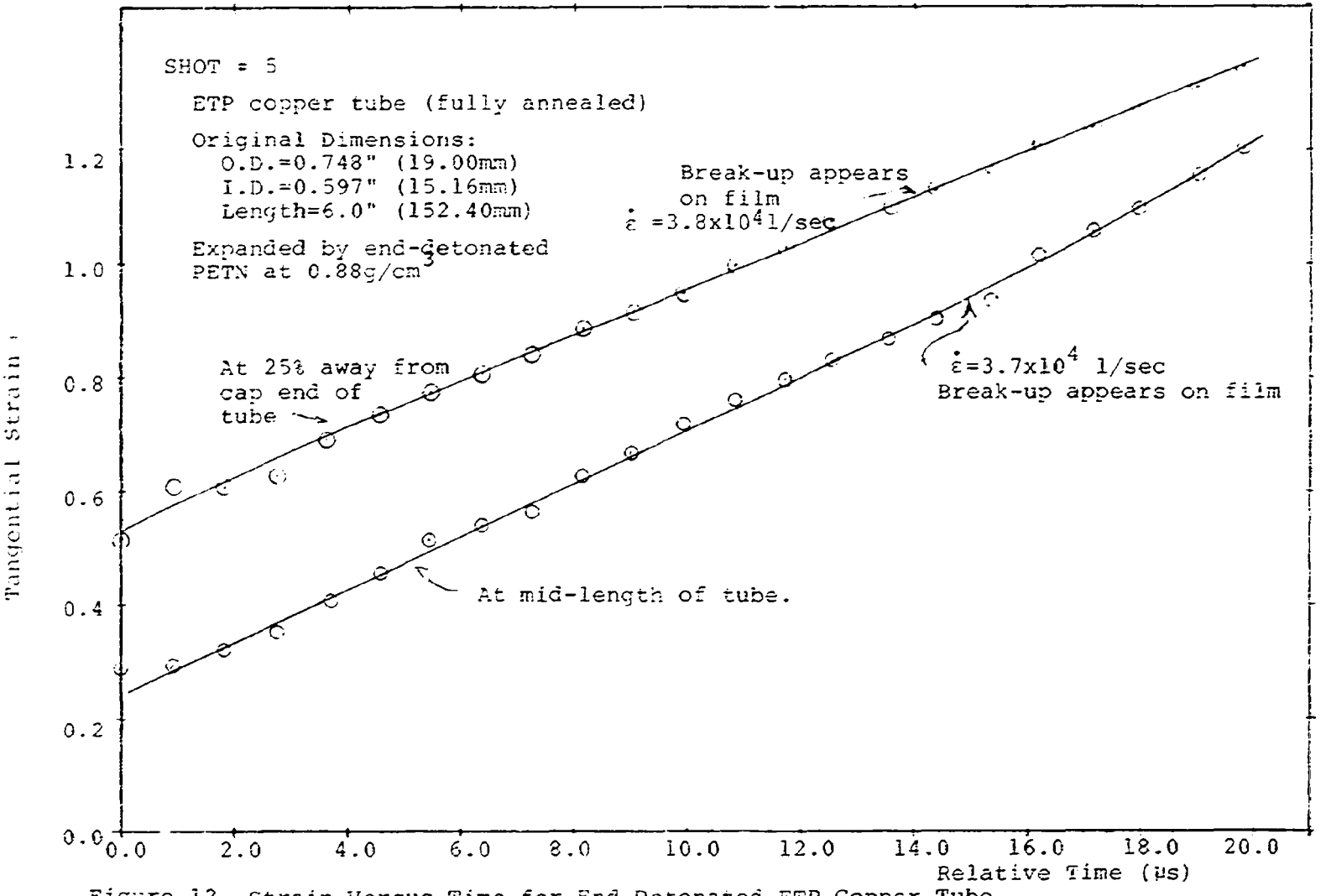

Figure 12. Strain Versus Time for End-Detonated ETP Copper Tube.
Time equal to zero is first readable frame of film record

Figure 13. Recovered Fragments From a High Strain Rate Experiment

TABLE 3

UDRI EXPLODING TUBE DATA

Shot #	ORIGINAL O.D. (mm)	ORIGINAL I.D. (mm)	Failure O.D. (mm)	Average Ultimate Strain $\bar{\varepsilon}_f$	Necked Ultimate Strain ε_f	Strain Rate $\dot{\bar{\varepsilon}}$ (1/sec)
0 OHFC Prima-Cord	19.05	15.75	32.25	0.53±.04	068±.05	$1.1\times10^4\pm.05\times10^4$
2 OFHC Prima-Cord	19.05	15.75	33.35	0.61±.05	0.65±.06	$1\times10^4\pm.1\times10^4$
5 ETP End-Detonated PETN @.88 g/cm^3	19.00	15.16	63.08	1.07±.10	1.52±.12	$3.7\times10^4\pm.3\times10^4$
6 ETP Prima-Cord	19.00	15.16	32.60	0.56±.04	0.68±.06	$0.9\times10^4\pm.05\times10^4$
7 ETP End-Detonated PETN @ ∿0.7 g/cm^3	19.00	15.16	51.69	1.00±.1	1.43±.12	$2.2\times10^4\pm.2\times10^4$
10 PETN Quasi-Uniform Detonation PETN @ 0.88 g/cm^3	19.00	15.16	57.15	1.1±.1	1.37±.11	$2.9\times10^4\pm.3\times10^4$

Circumferential fiducial lines were drawn at midlength on two of the tubes (Shot No. 0 and Shot No. 7) prior to the experiments. By measuring the distance between the lines before and after the experiment, the axial elongation of the tubes was determined to be $\sim$3 percent. This value was consistent for both the tubes tested, one with a strain rate at failure of $1 \times 10^4 s^{-1}$, and the other at $2.2 \times 10^4 s^{-1}$.

The framing camera field of view was as sketched in Figure 7b. All the exploding tube data appearing in Tables 2 and 3 are based on measurements made at the midlength of the cylinder. This was done to prevent end effects from being considered in the results. Examination of the films do not indicate that any end related phenomena were significant at tube midlength. Osborn of AFATL has carried out a TOODY calculation for a uniform axially expanded cylinder with approximately the same dimensions as the UDRI cylinders[14] (i.e., OD = 21.6 mm; wall thickness = 1.27 mm; length = 152 mm; 0.88 g/cm^3 PETN explosive). Figure 14 shows a velocity vector plot of half the cylinder surface at 15 μs after the beginning of detonation. This plot clearly shows that end effects at the midlength position on the tube are negligible.

Achieving simultaneous uniform axial detonation in the UDRI tests turned out to be very difficult, resulting in ultimate strain dependence on axial location previously noted. Instead of having a right circular cylinder at anytime during the expansion, a conical shell was formed with a total included angle of 14° to 20° at failure. Due to this cone angle, the tube was not in a state of uniform axial expansion. Thus, ε_z, the axial strain, was not equal to zero at failure, but can be calculated from:

$$\varepsilon_z = \frac{1}{2} \left(\frac{du}{dz}\right)^2$$

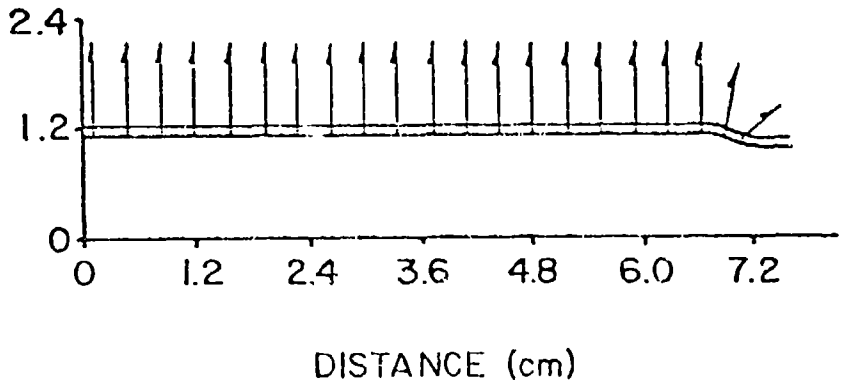

Figure 14. Calculated Velocity of Copper Cylinder after 15 μs, Reference 14

a Lagrangian component of strain. For small strains this may be written as:

$$\epsilon_z = \frac{1}{2} \left(\frac{\Delta u}{\Delta z}\right)^2$$

where Δu is change in displacement of the cylinder wall over a length along the cylinder axis, Δz. Thus,

$$\Delta u / \Delta z = \tan \theta$$

and

$$\epsilon_z \sim \frac{1}{2} (\tan \theta)^2$$

where θ is half the angle formed by the conical tube. The equation relies on the assumption that waves transmitted from the end of the tube do not cause axial strain relief. The

bulk sound speed in copper, 3.9 mm/μs, is probably a good estimate of extensional wave speed in the expanded material. Wave transit time from end to end of the cylinder (152 mm long) is ∿38 μs. The total expansion time to failure of the higher strain rate cylinders is ∿20 μs and for the lower strain experiments ∿40 μs. Thus, for the higher strain rates, end relief is probably minimal, while some relief does occur in the lower rate tests. The extent to which these waves effect the test is not clear. For a maximum cone angle of 20°, the axial strain ε_z will be 0.015 or about one-half the measured value, based on the fiducial lines previously noted. This strain is quite small relative to the radial and tangential strains, and probably has insignificant effects. The expansion of the tubes at strain rates ∿1 x $10^4 s^{-1}$ was very uniform along the tube length. Total included cone angle did not exceed ∿2 degrees, except for end effects already discussed. This uniformity is due to the smoothing of the pressure inhomogeneities by the oil between explosive and cylinder wall. Thus, these tests most closely approach plane strain conditions.

3.4 HARDNESS MEASUREMENTS

Microhardness measurements were made on sectioned/polished specimens using the standard Vicker-Hardness test procedure with a 50 g load. The results of these measurements are shown in Table 4. The hardness appears to be closely related to strain and strain rate.

One series of hardness measurements was made in regions of "uniform" strain, and another set was made in the necked region only. The same hardness was found in both uniform and necked regions of the expanded tubes. (Since no distinguishable patterns of hardness between uniform and necked regions could be found in the cylinders, all values were used in calculating the mean and standard deviation values of Table 4.) There was very little scatter in hardness of the

TABLE 4

VICKERS MICROHARDNESS OF STRAINED SPECIMENS OF ETP COPPER

Specimen Strain Rate (s^{-1})	Vickers Hardness in Uniform Strain Region*	Vickers Hardness in Necked Region†*	Standard Deviation of Measurements
Stock Material after annealing	66.5	-----	3.8
4×10^{-4} quasistatic tensile	68.7	75.7	5.0
4×10^{0} quasistatic tensile	73.0	85.0	5.0
1×10^{3} Hopkinson bar tensile	84.0	103.0	5.0
1×10^{4} exploding tube	99.4	99.4	3.9
2.5×10^{4} exploding tube	145.1	145.1	4.7

†For the tensile specimens hardness measurements in the necked region were made not more than 0.25 mm from the fracture surface. The larger standard deviation is due to the relatively small area on which measurements could be made.

*For the tube fragment specimens measurements were made near fracture surfaces and in the bulk material with no distinguishable differences in hardness measurements.

cylinders, as can be seen from the small magnitude of the standard deviations. The standard deviation for the tensile specimens was higher than that for the tube fragments due to the relatively small number of reliable measurements which could be made in the necked region of these specimens.

There were consistent variations in hardness between uniformly strained and necked regions of the tensile specimens. The difference between the uniform hardness of the tube specimens and the location-dependent hardness of the tensile specimens suggests that a nonlocalized diffuse straining of the tube specimens existed until very late in the expansion. In the tensile specimens localized straining began very soon after the yield stress was exceeded.

3.5 METALLOGRAPHIC STUDIES

A specimen or fragment was sectioned and polished for each strain rate specimen tested. The specimens were etched and photomicrographs were made. All of the tensile specimens were sectioned such that the longitudinal axis of the specimen lay in the section plane. Figure 15 shows the $4 \times 10^{-4} s^{-1}$ strain rate specimen at the necked region and in the uniformly strained region. There is very little grain elongation in the uniformly strained region, even when compared to the fully annealed sample specimen shown in Figure 16. Figure 17 shows much the same results for the $4 \times 10^{0} s^{-1}$ strain rate specimen. Figure 18 shows photomicrographs of the split Hopkinson bar tensile specimen. The uniformly strained section is quite similar to the specimens from lower strain rates. However, in the necked region a dramatic increase in the number of voids which have coalesced is apparent. The void growth process appears to be dependent on strain rate.

The tube fragments were sectioned on a plane perpendicular to the longitudinal axis of the tube. Figure 19a shows a photomicrograph of a tube fragment from a $1 \times 10^{4} s^{-1}$ strain

strain direction

(a) uniformly strained region magnification: 120X

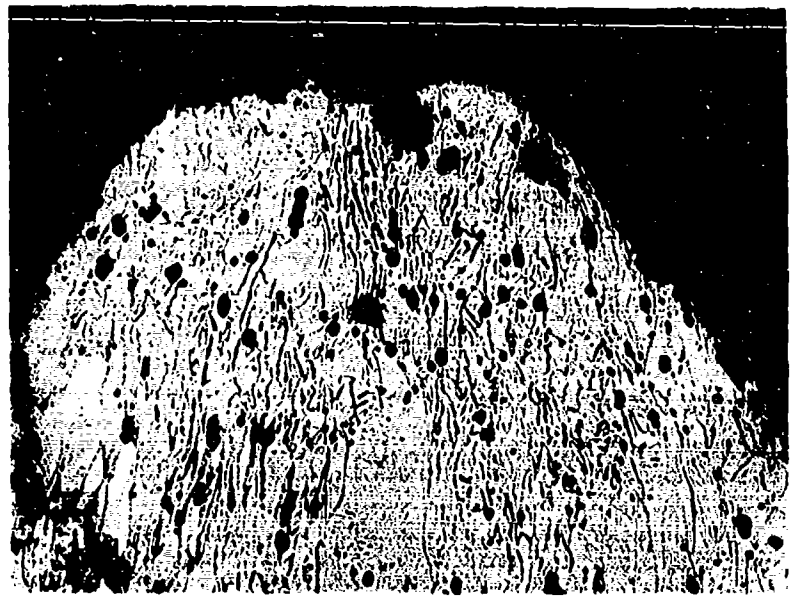

strain direction

(b) tip of neck magnification: 100X

Figure 15. Photomicrograph of 4 x $10^{-4}s^{-1}$ Tensile Specimen

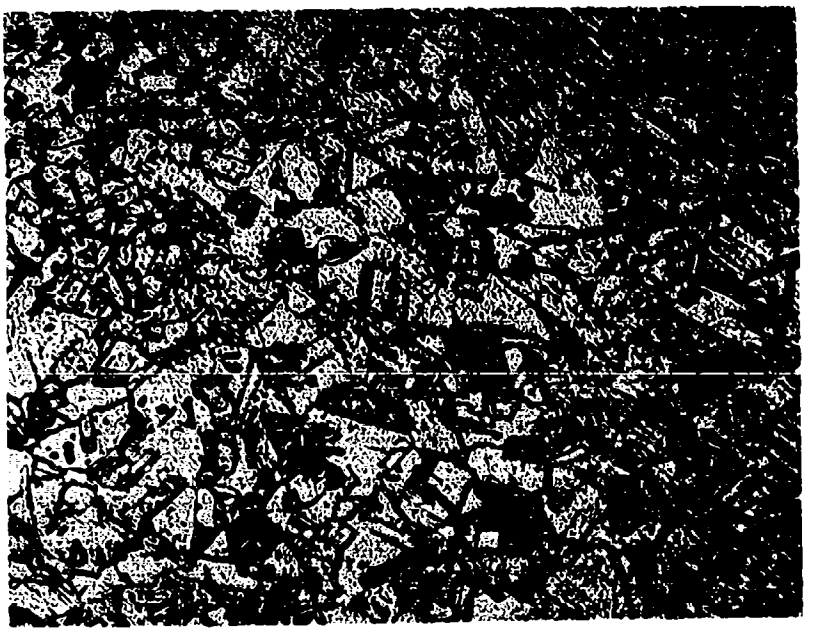

Figure 16. Photomicrograph of Fully Annealed Stock Specimen (no straining after anneal). magnification: 100X

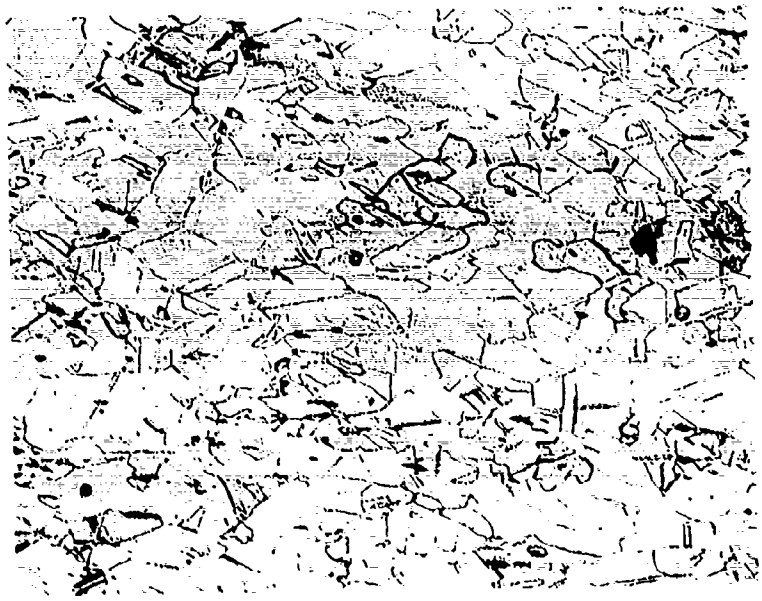

strain direction

(a) uniformly strained region magnification: 120X

strain direction

(b) tip of neck magnification: 120X

Figure 17. Photomicrographs of 4 x $10^0 s^{-1}$ Tensile Specimen

strain direction

(a) uniformly strained region magnification: 120X

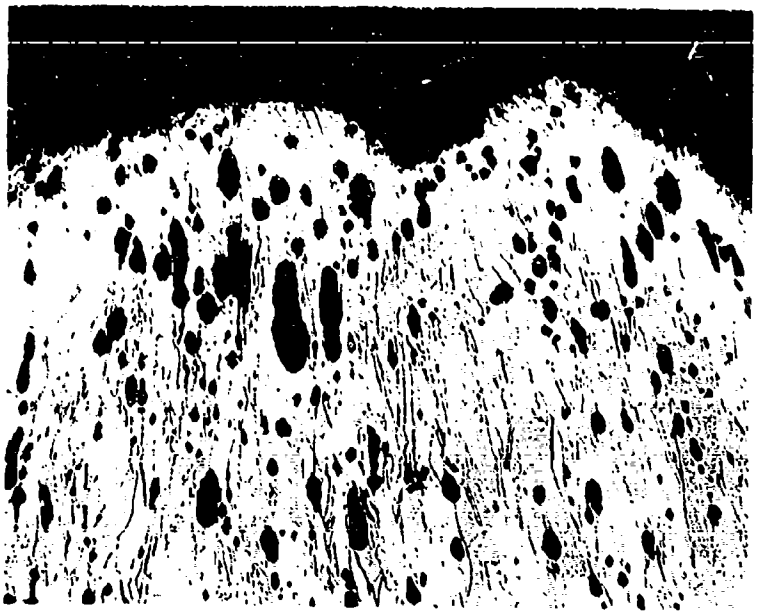

strain direction

(b) tip of neck magnification: 100X

Figure 18. Photomicrographs of 1 x $10^{3}s^{-1}$ Tensile Specimen

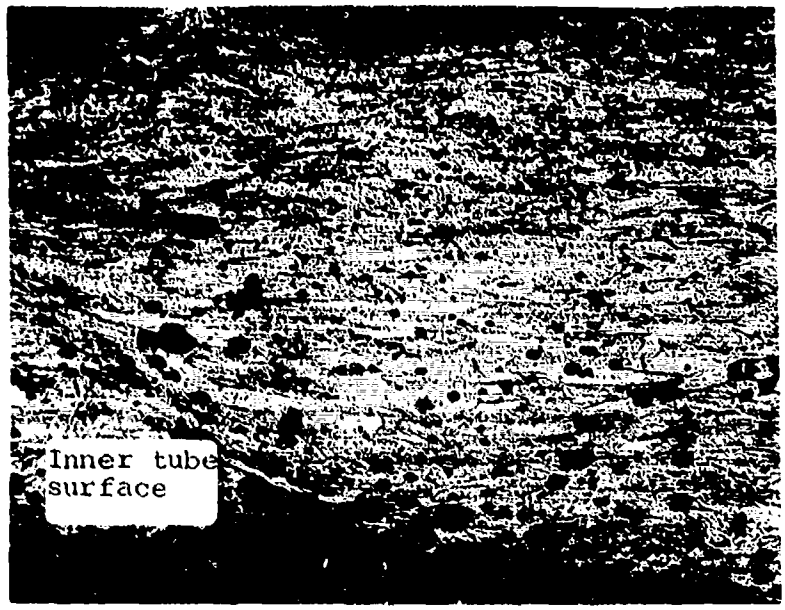

strain direction

(a) 1 x $10^4 s^{-1}$ tube specimen magnification: 120X

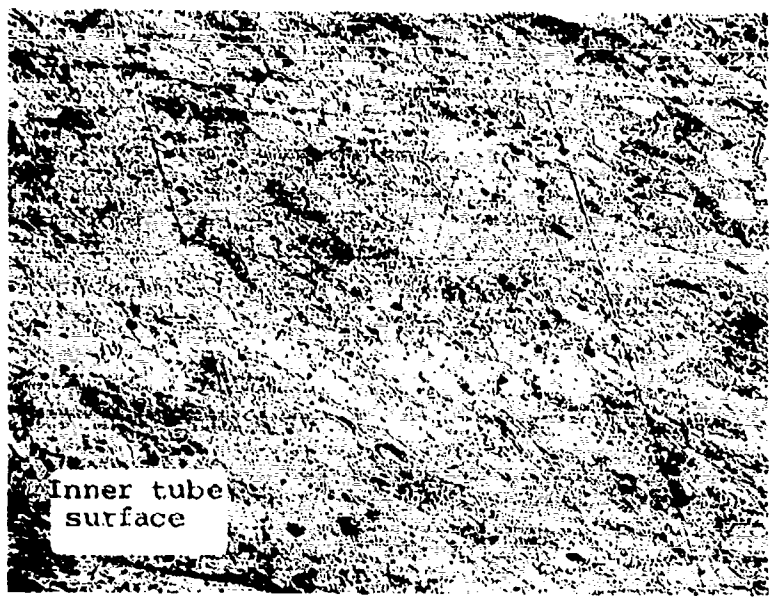

strain direction

(b) 2.4 x $10^4 s^{-1}$ tube specimen magnification: 120X

Figure 19. Photomicrographs of Exploding Tube Fragments

rate experiment. Comparing these two micrographs a significant difference may be noted. In the higher rate experiment, voids have coalesced to form pores about 25 μm across. Much less coalescence has occurred in the $1 \times 10^4 s^{-1}$ specimen in which the largest voids are about 5 μm in diameter. The other notable feature of Figure 19b is the higher concentrations of voids at the inside wall surface. This feature will be discussed in the next section.

One effect undergone in the PETN filled cylinders, not seen in the Prima-Cord loaded tubes or the tensile specimens, is an externally applied temperature gradient. In the Prima-Cord tube the oil provides sufficient insulation between hot explosive products and tube wall to make temperature effects negligible. However, the PETN tube wall is exposed directly to the hot explosive products which have typical peak temperature ~3000°K. Simple calculations have been carried out to estimate the temperature distribution in the tube wall. The results of these calculations are shown in Figure 20. The upper curve in this figure is the temperature distribution after 20 μs exposure to a 3000°K temperature source and the lower curve gives the temperature distribution after a 20 μs exposure to a 1084°K temperature heat source. The higher temperature corresponds to typical explosive plane temperatures while the lower temperature is the melting temperature of copper. Since the temperature of the explosive products falls quite rapidly during an expansion, the actual temperature distribution in the copper will probably be between the two. However, no indication of melting is seen in the photomicrographs, indicating that the lower temperature distribution in Figure 20 is more nearly correct. Even for the lower curve, temperature effects need to be considered in an analysis of the failure mode.

The final fracture in all specimens occurs across a concentration of voids as seen in Figure 15 for a tensile specimen and in Figure 21 for the shear failure of a tube specimen. Similar results have been found by other researchers at lower strain rates in steel and other materials[15,16].

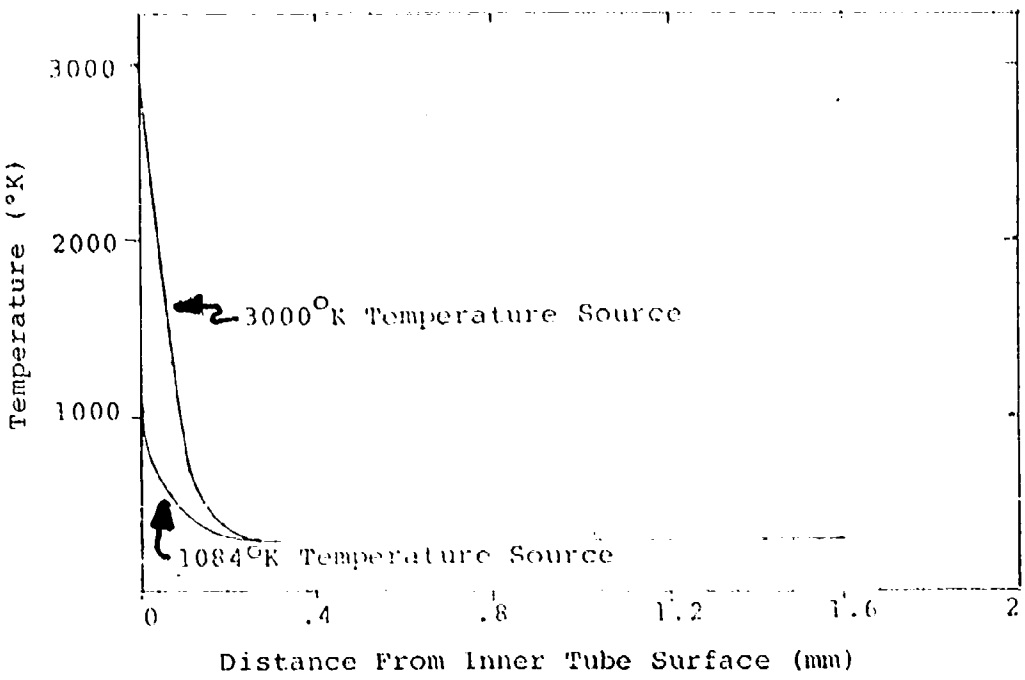

Figure 20. Temperature Distribution in Copper Tube Wall After 20×10^6 Exposure to Indicated Temperature

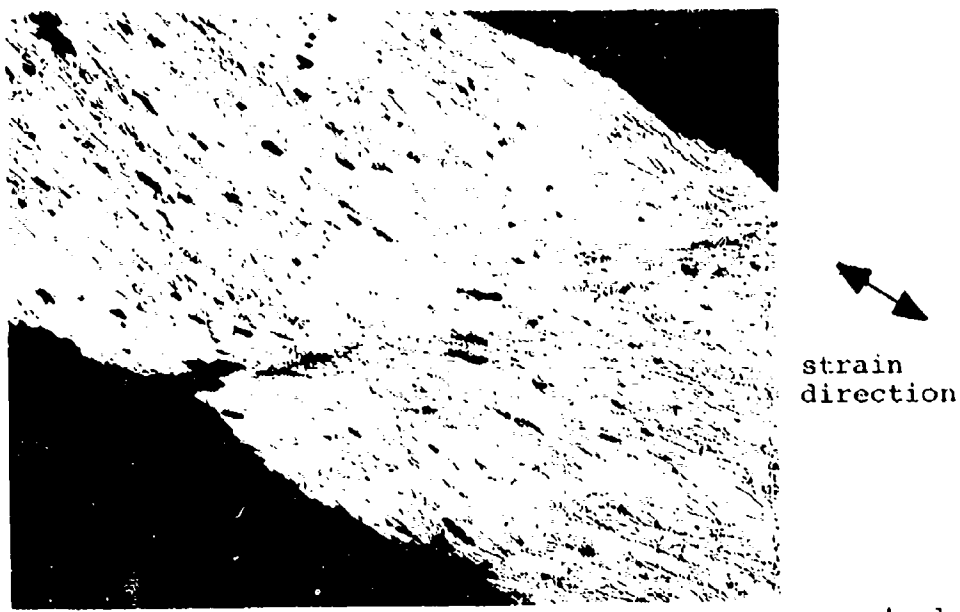

Figure 21. Incipient Shear Failure Across Voids in $2.4 \times 10^4 s^{-1}$ Tube Specimen

3.6 ULTIMATE STRAIN VERSUS STRAIN RATE

Figure 22 is a plot of the ultimate strain against strain rate for all the experiments shown in Tables 1, 2, and 3. The strains plotted in this figure are average values, which do not take necking into account. The average ultimate strain apparently is not significantly affected by rate of strain below approximately $10^3 s^{-1}$. However, between 10^3 and $10^4 s^{-1}$ the dependence is shown to be very substantial for both ETP and OFHC copper.

Another notable feature revealed by this graph is that OFHC copper has a greater ultimate strain at the high strain rates. At lower strain rates, there appears to be no difference between ETP and OFHC ultimate strain.

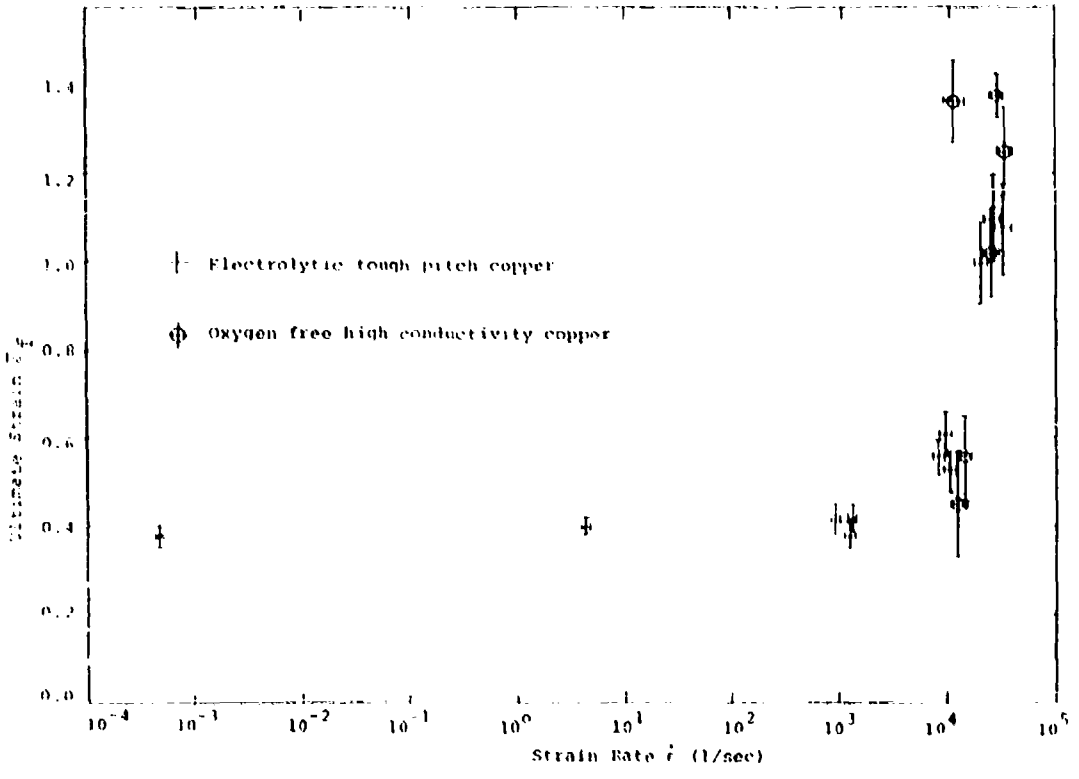

Figure 22. Plot of Average Ultimate Strain Versus Strain Rate for Fully Annealed ETP Copper and OFHC Copper. Data from standard tensile tests; split Hopkinson bar tests; and exploding cylinder tests.

A plot of ultimate strain in the necked region versus strain rate is shown in Figure 23. These data are for ETP copper only and include the diameter measurements on failed tensile specimens, and thickness measurements on expanded cylinder fragments. Figure 23 shows that as the strain rate is increased, more bulk material is involved in the straining process.

Necking is apparently suppressed causing strain to be distributed more evenly through the material, allowing higher ultimate strains to be achieved. Final fracture occurs through a neck, which is bound to develop. Further discussion of the mechanisms which could suppress necking are discussed in the next section.

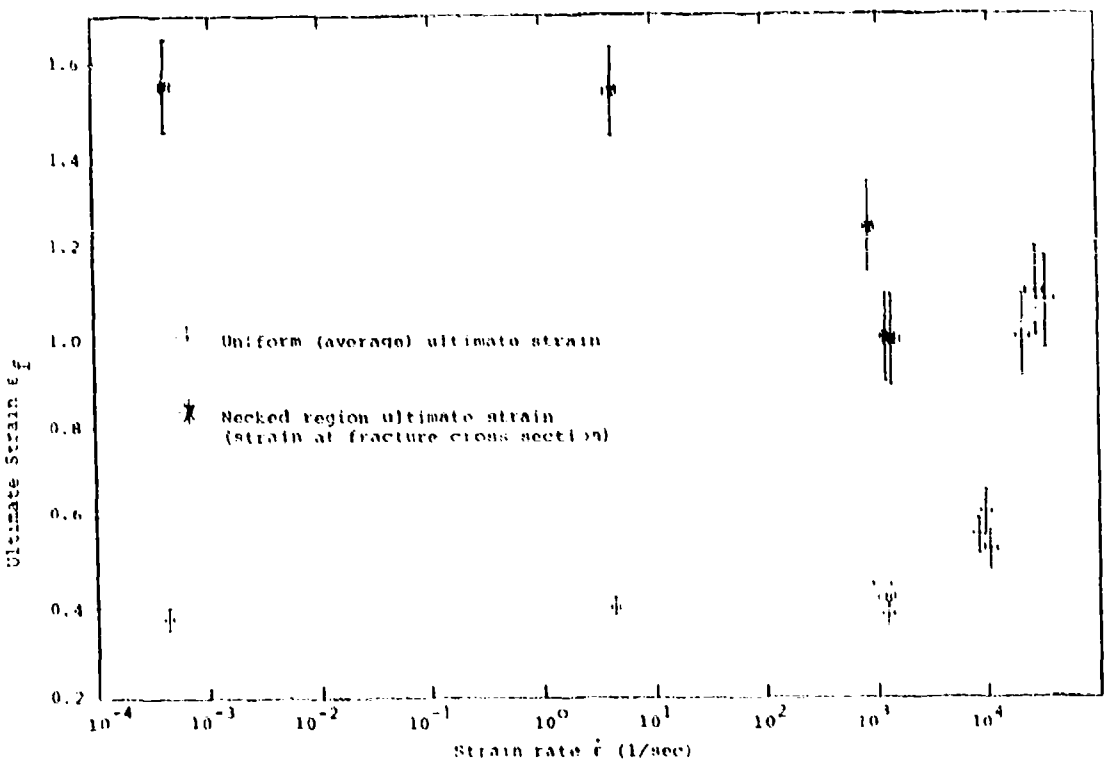

Figure 23. Plot of Average Ultimate Strain and Ultimate Strain in Necked Region Versus Strain Rate for Fully Annealed Electrolytic Tough Pitch Copper

SECTION IV
DISCUSSION OF RESULTS

4.1 FAILURE MODES

4.1.1 Tensile Specimens

Figure 8 shows a typical failed tensile specimen from the tests at $\sim 1\ s^{-1}$ strain rates. Failure of these specimens always occurred at approximately midlength; this reassures us that failure was not induced by end effects. The failure appears to be ductile fracture following initial necking by plastic deformations. The final fracture surface is inclined to the longitudinal axis of the specimen at an angle of ~ 37 degrees. Careful examination of the appearance of the fracture surfaces of these specimens indicates a "cup and cone" type final fracture. The surface has a coarsely granular structure with little or no evidence of burnishing. The fracture surfaces for the $10^{-4}s^{-1}$ and the $10^{0}\ s^{-1}$ strain rate specimens appear to be very similar.

4.1.2 Hopkinson Bar Specimens

Late time compressive waves in the split Hopkinson bar apparatus caused the ends of the failed specimen to bounce together. The resulting deformation of the specimen ends was relatively minor, but it defeated meaningful study of the $10^{3}s^{-1}$ fracture surface.

4.1.3 Exploding Tube Specimens

Failure of the expanded tubes occurred by longitudinal fracture. The fragment size depended on the strain rate of the expansion. As discussed previously, tests may be roughly categorized as high ($3 \times 10^{4}s^{-1}$) or low ($10^{4}s^{-1}$) strain rates depending on whether, respectively, the

charge was granular PETN or Prima-Cord in oil. The largest fragments from the low strain rate experiments were ∿28 mm in the longitudinal direction by ∿12 mm circumferentially. The smallest fragments measured only a millimeter or less in width. In the high strain rate tests all the fragments were millimeter size or less. These fragments are shown in Figure 13. The number of fragments produced by the high strain rate tests was impossible to measure because of their small size and the difficulty of 100 percent recovery; however, the number certainly exceeded 200. On the other hand, the 1 x $10^4 s^{-1}$ fragments numbered not more than ten.

Examination of the low strain rate fragments revealed the surface instabilities, or wrinkles, which can also be seen in Figure 24. There were two distinct size scales to the wrinkles. One set was 4 - 5 mm and the other slightly sub-millimeter. Failure was associated with the larger wrinkles.

In all cases the fracture began on the outside surface of the tube. On the 1 x $10^4 s^{-1}$ tubes the dimpling associated with necking was chiefly on the outside surface. As indicated in Table 3 and Figure 23, very little necking occurred before failure of these tubes.

On the 3 x $10^4 s^{-1}$ fragments the cracks initiated at the outside surface. The cracks initially appeared in the valleys between the larger (4-5 mm) wrinkles. Necking at the fracture involved a very small amount of material; the width of the necked region was at most two wall thicknesses in the circumferential direction. As indicated in Figure 23, the wall thickness in the necked regions was reduced to about 0.6 of the wall thickness of the bulk material.

The failure surfaces on the 1 x $10^4 s^{-1}$ specimens were roughly on an angle approximately 45 degrees to a normal to the specimen surface. The fracture surface was usually a single shear plane, running all the way across the wall of the tube from outside to inside. The shearing surfaces had a

Figure 24. Fragments from a 1 x $10^4 s^{-1}$ Exploding Tube Experiment

castellated, coarsely granular structure with no indication of burnishing.

Somewhat different features were observed in the highest rate expansions, $\sim 3 \times 10^4 s^{-1}$. The fracture surfaces were on a steeper angle, approximately 60 degrees, to the surface normal. The surfaces were also generally a single shearing plane running completely across the tube wall. The surfaces had a definite shear-slip appearance, e.g., they were drawn to a very thin shear-lip at the surface. A moderately burnished appearance is notable for this surface.

4.2 DISCUSSION OF FAILURES

It is apparent from the preceeding discussion that more than one failure mode was activated in these tests. This section contains a general discussion of mechanisms which

could effect the strain to failure. Several factors, including strain and strain rate will be discussed which are likely to have significant effects on ultimate strain.

4.2.1 Strain Hardening

In general, the condition necessary to initiate an instability (thus, a failure) in the uniform flow of metal, requires that the next increment of strain-induced hardening be negated by an accompanying strain-induced softening. When this occurs, further straining will tend to concentrate at the location where the resistance to flow was first lost with very little strain distributed throughout the bulk material. The ultimate strain measurements appearing in Figure 22 ($\bar{\varepsilon}$ versus $\dot{\varepsilon}$) are useful for determining maximum uniform strain which may be expected in other high deformation processes.

Strain hardening may be due to many factors. Its effect is to cause an increase in the flow stress, σ, for a strain increment $\Delta\varepsilon$. The derivative with respect to strain of flow stress is $d\sigma/d\varepsilon$. Since σ is, in general, a function of strain, strain rate, temperature, surface energy, etc., (i.e., $\sigma = \sigma[\varepsilon\ \dot{\varepsilon},\ T,\ \gamma,\ldots]$) we may write

$$d\sigma/d\varepsilon = \frac{\partial\sigma}{\partial\varepsilon} + \frac{\partial\sigma}{\partial\dot{\varepsilon}}\ \frac{d\dot{\varepsilon}}{d} + \frac{\partial\sigma}{\partial T}\frac{dT}{d\varepsilon} + \frac{\partial\sigma}{\partial\gamma}\frac{d\gamma}{d\varepsilon} + \ldots\ldots \qquad (5)$$

Any term on the right of this equality which becomes sufficiently negative in magnitude can be the source of an instability condition. For metals, the first three terms on the right-hand side of the equation usually dominate.

For the tensile specimens at low strain rates, the strain hardening is due to the $\frac{\partial\sigma}{\partial\varepsilon}$ term. The onset of an instability begins when further increases in strain occur with no further increases in load (i.e., $\frac{dF}{d\varepsilon} = 0$). The load-carrying ability of the specimen is $F = TA$, where A is the area on which the stress T acts. The instability condition gives

$$A \frac{\partial T}{\partial \epsilon} = -T \frac{\partial A}{\partial \epsilon}$$

with

$$d\epsilon = \frac{dA}{A}$$

necking in the tensile specimens will initiate when

$$\frac{dT}{d\epsilon} = T. \tag{6}$$

Thus, necking for tensile specimens at low strain rates is closely related to geometric changes.

Strain hardening at low strain rates has been described several ways, but the most widely used seems to be the power law relationship

$$\sigma = K\epsilon^n \tag{7}$$

where K is a "flow stress" and n is the strain hardening exponent. Backofen[17] describes this and other relationships for stress-strain hardening. From Equations (6) and (7) an instability will occur when

$$\epsilon = n. \tag{8}$$

Values of K and n for an annealed copper are 3.2 Kbar and 0.54, while for an annealed and tempered 0.05 percent C steel sheet K = 5.0 Kbar and n = 0.23.[18] These numbers indicate that copper undergoes more strain hardening than steel for the same amount of strain.

Comparing Equation (8) with Figure 22 it appears that influences other than strain hardening are negligible to $10^3 s^{-1}$ strain rates. Equation (7) can be used at these lower strain rates to give approximate description of the stress-strain curve.

Tubular steel bomb casings, driven radially outward by high explosive detonation pressures, possess certain similarities to the exploding cylinders used in these ultimate strain tests. Taylor[19] devised models to describe bomb dynamics and Hoggatt and Recht[20] studied the influence of stress state on the deformation and fracture behavior of bomb casings. The model used by these investigators is based on the effects of the compressive hoop stresses in the cylinder wall during expansion. These stresses are due to the explosive pressure and the inertia associated with the tube wall movement at the beginning of motion. At the beginning of the expansion event, compressive hoop stresses extend to the outside surface of the tube. As the expansion continues, the magnitude of the compressive hoop stresses diminish, first at the outer surface. Gradually, the hoop stresses become tensile. Thus, a boundary between regions of compressive and tensile hoop stress moves inward across the tube wall as the expansion progresses. The position of the zero hoop stress boundary at any point in the expansion process is mainly dependent on the detonation pressure and the mass of the tube. During the expansion, the radial stress component is compressive, equal to the detonation pressure at the inner tube surface and falling to zero at the outer surface. The axial stress in the tube is at first compressive, due to shock waves in the tube. The axial stresses fall to nearly zero very early in the expansion. Osborn's[14] TOODY calculations for a uniformly expanded tube support these generalizations. Stress calculations from the TOODY program are shown in Figure 25 for a 21.6-mm OD by 1.27-mm wall thickness by 152-mm-long copper tube expanded by 0.88 g/cm^3 PETN detonation pressures. These plots of stress are for a point at the

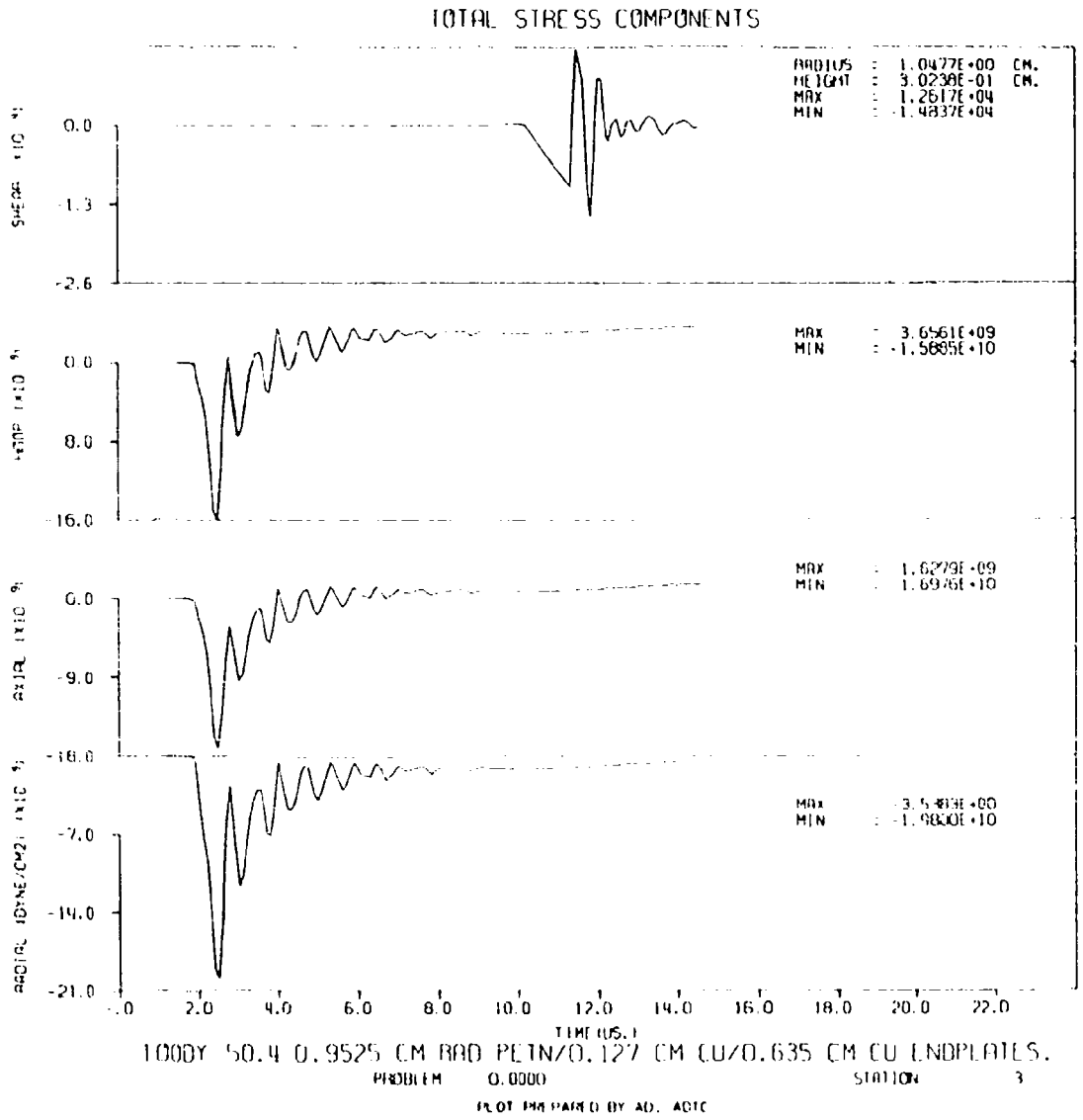

Figure 25. Calculated Stress Components in Copper Cylinder Expanded by PETN (Reference 14)

midlength in the tube 0.32 mm from the outside surface. Thus, the tube experiences highly triaxial nonconstant stress states during the expansion.

One consequence of the existence of compressive hoop and radial stresses on the inner portion of the tube wall is that fracture must begin on the outside surface, and at anytime of the expansion fractures may only penetrate to the boundary between tensile and compressive hoop stresses. This theory is supported not only by evidence from the present tests, but by work of Taylor[19], Famiglietti[21], Allison and Schriempf[22], and Hoggatt, et al.[20] Taylor suggested the fractures would be radial, but Hoggatt and Recht described fractures occurring on shear planes described for the present tests in Section 4.1.3. The radial fractures described by Taylor occur for very low order detonations as discussed by Hoggatt and Recht.[20]

The expansion process is diagrammed schematically in Figure 26. The model predicts fractures to extend no further inward from the outside tube surface than the boundary where the tensile hoop stress is equal in magnitude to the compressive radial stress. Expansion in the compressive hoop zones takes place by a process of extrusion while in the tensile hoop region, fractures occur. This takes place when the tensile hoop stress becomes equal in magnitude to the compressive radial stress. Complete fracture is predicted when the tensile hoop stress equals the radial stress at the inside surface of the tube.

Hoggatt and Recht[20] developed a model to predict the location of the compressive/tensile boundary as a function of tube radius, based on the equation of motion for the tube and assuming isentropic expansion of the detonation gases. Figure 26 is based on this development, and is the result for a mild steel tube (50.8-mm ID by 6.35-mm wall thickness expanded by RDX explosive with a Chapman-Jouquet pressure of 157 Kbar). The theory predicts failure radius to within nine percent of experimental values for mild steel.[20]

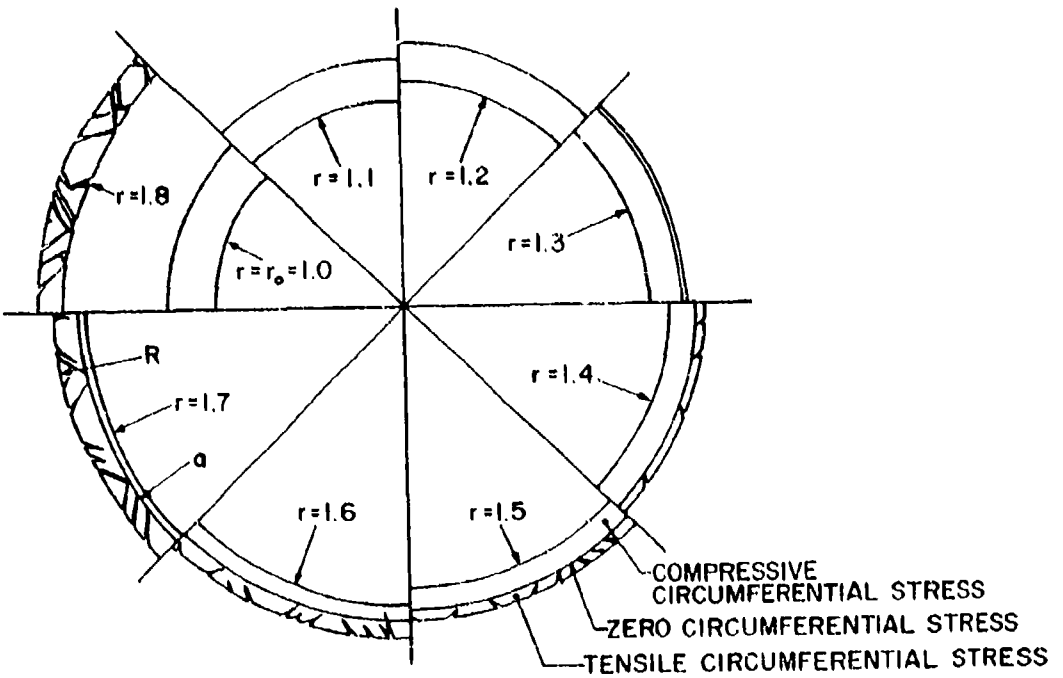

Figure 26. Fracture of Explosively Expanded Cylindrical Tube [20]

Hoggatt and Recht's model was used to estimate the failure radius for the copper tubes of the present study. For the steel tube the calculations agree with the findings of Hoggatt and Recht, (i.e., failure strain = 0.44). For the copper tube, failure is predicted at a strain approximately 0.5 for the PETN filled cylinders and 0.37 for the Prima-Cord shots. These calculated values are significantly lower than those found in this program, as shown in Table 3. Two factors may explain the excursion of theoretical results from experimental findings. These two factors include explosive loadings incorrectly modelled and failure of the model to account for all strain hardening effects. First, the loading effects will be discussed with the strain hardening effects delayed until later.

With the low density PETN, the Chapman-Jouquet (CJ) pressure is approximately 70 Kbar. This value is less than half the CJ pressure for the RDX modelled by Hoggatt and Recht. Also, the mass ratio of initial loadings of PETN to RDX is 0.09 and for the Prima-Cord to RDX loading it is 0.006. The model predicts fracture from outside surface to the radius where $|\sigma_\theta| = |\sigma_r|$. With the substantially smaller loads of the UDRI tests, the compressive/tensile boundary will move across the wall thickness after lower radial expansions causing the tube to go into a state of tensile hoop stress earlier, at which time the model predicts failure. The higher density loadings used by Hoggatt and Recht caused acceleration of the tube during much, if not all, the expansion, thus delaying tensile hoop stresses until deformations had occurred. Although failure in the steel tubes may be modelled with this theory, it does not do well for copper.

Although the model does not accurately predict failure in the copper tubes, it does focus attention on the importance of the initial compressive stress and strain states, on the subsequent tensile straining of the material. Relative to the steel, the copper tubes would tend to undergo more strain hardening in the early stages of expansion. The effect of strain hardening is to cause the $\frac{\partial \sigma}{\partial \epsilon}$ term on the right-hand side of the $\frac{d\sigma}{d\epsilon}$ strain hardening Equation (5) to become more positive. Strain hardening during early stages of tube expansion, when stresses are compressive, will also cause a positive increase of the $\frac{\partial \sigma}{\partial \epsilon}$ term. This increase will tend to diminish or delay negative effects of the other terms, thus increasing $\frac{d\sigma}{d\epsilon}$. Physically, the strain hardening will cause a more even distribution of the stress and strain in the tube wall. The net effect is to cause more uniform tensile flow before failure, by suppressing instabilities.

The higher concentration of voids at the inside surface of the tube wall as shown in Figure 19 may be explained by consideration of the high triaxial stress state and the

extrusion which takes place there. Hancock and Mackenzie[3] have an in-depth examination of this process for steel, but the analysis may be applied to any ductile material.

Basically, the voids would be expected to nucleate from the high number of CuO_2 inclusions usually present in ETP copper. The subsequent coalescence of these voids during further straining would be related to stress and strain rate by[3]

$$\frac{dR}{R} = 0.28\ d\varepsilon^P \exp\ (3\sigma_m/2\bar{\sigma})$$

where

R is the mean hole radius
$d\varepsilon^P$ is the plastic strain increment
σ_m is the mean or hydrostatic stress
$\bar{\sigma}$ is the deviatoric portion of the stress.

Hancock and Mackenzie assume that the failure strain is inversely proportional to hole growth rate, to give

$$\varepsilon^f = \alpha \exp\ (-3\ \sigma_m/2\ \bar{\sigma})$$

where

ε^f is failure strain
α is a material constant

Thus, for the high triaxial state of stress in the tube wall, hole growth rate would be predicted to be high. Also, the more nearly uniform distribution of the voids in the $1 \times 10^4 s^{-1}$ strain-rate fragments is possibly due to the much less severe triaxial stress state and shorter duration of the stress state for these specimens.

This conclusion may be used, at least qualitatively, to explain the higher ultimate strains measured in the LLL results, shown in Figure 22. The ratio of the explosive loading energy in the UDRI experiments to those of LLL is at most 0.35, and as small as 0.09. Thus, for the LLL experiments the tubes should have undergone more compressive strain hardening and therefore larger ultimate tensile strains would be expected.

4.2.2 Strain-Rate Hardening

The second term $\frac{\partial \sigma}{\partial \dot{\varepsilon}} \frac{d\dot{\varepsilon}}{d\varepsilon}$ in the strain hardening equation is the strain-rate hardening term. Both parts of this term are normally positive and thus the term is a source of instability resistance. $\frac{\partial \sigma}{\partial \dot{\varepsilon}}$ is positive because stress normally increases with strain rate and $\frac{d\dot{\varepsilon}}{d\varepsilon}$ is positive because of geometrical changes as the neck begins to form.

Most strain-rate hardening theories have been developed for 'creep' conditions.[17] These theories are usually based on some dislocation theory of slipcreep or on diffusional flow theories of single atoms. These theories are more appropriately applied to strain rates of 10^0 s^{-1} and less.

Kumar and Kumble[3] used a compressive split Hopkinson bar apparatus to load OFHC copper specimens to strain rates above $10^3 s^{-1}$. They found that the strain hardening sensitivity of copper may be divided into two regions.

1) A thermally activated region below $10^2 s^{-1}$ strain rates, and

2) A viscous damping region above $10^3 s^{-1}$ strain rates.

Kumar and Kumble correlate their experimental results with a theory of viscous phonon drag, at high strain rates (i.e., $10^3 s^{-1}$). In this theory, phonons are considered a source of dislocation damping. Thus, strain rate effects are directly related to dislocation mobility and the density of mobile dislocations in the metal. This dislocation mobility

is explained in terms of a dislocation multiplication and annihilation mechanism. Mobile dislocations are multiplied when collision with fixed dislocations occur. Annihilation happens when a mobile dislocation meets another mobile or higher energy fixed dislocation. A linear relationship between flow stress and strain rate was found in this higher strain-rate ($>10^3 s^{-1}$) viscous damping region.

In the UDRI experiments as in those of Kumar and Kumble, the viscous damping mechanism has an effect to more evenly distribute stresses in the material by delaying local concentrations of dislocation pile-up until late very high strains are reached.

Physically, when strain-rate hardening occurs it has the same effect as strain hardening. That is, it increases the magnitude of the flow stress thus causing a tendency to prevent necking. This effect may be used to describe the increase in neck length observed from the $4 \times 10^{-4} s^{-1}$ strain rate tensile specimen to the $1 \times 10^3 s^{-1}$ strain rate split Hopkinson bar specimen. It would also follow that the increased hardness of the higher rate tensile specimens is due to strain rate hardening, since ultimate strains are approximately the same as in the low rate samples. The increased hardness of the tube specimens is likely due to a combination of strain and strain rate hardening effects.

4.2.3 Thermal Hardening

The third term $\frac{\partial \sigma}{\partial T} \frac{dT}{d\varepsilon}$ of the hardening equation is usually negative, thus encouraging instability growth. Since the deformation work appears as heat $\frac{dT}{d\varepsilon}$ is positive. Usually, $\frac{\partial \sigma}{\partial T}$ is negative because with increasing temperatures more thermal agitation is applied to fixed dislocations, lowering the stress required for dislocation movement. This process of thermal agitation of dislocations is a more stable process when the agitation is localized, resulting in instabilities in the material.

Adiabatic shear processes normally occurring in metals at higher strain rates have not been observed in copper[16] due to the effects of strain and strain-rate hardening as previously described. The UDRI specimens do not show these failures which are usually characterized by very thin failure bands in high strain-rate processes.

The increased temperatures applied to the tubes as discussed in Section 3.5 would tend to increase ductility. However, the externally applied temperature increase is probably a second-order effect when compared to the strain and strain-rate hardening effects imposed at high strain rates. Until very late in the expansion process only an insignificant portion of the tube wall experiences high enough temperatures to affect mechanical properties.

SECTION V
CONCLUSIONS AND RECOMMENDATIONS

The results of this study clearly indicate that average ultimate strains of at least 1.1 may be obtained for strain rates (at ultimate strain) of $2.5 \times 10^{4} s^{-1}$. Significant increases may be observed at strain rates in the vicinity of $1 \times 10^{4} s^{-1}$.

In Figure 23 average ultimate strain and true ultimate strain are plotted against strain rate. From this figure one may observe that between strain rates of $4 \times 10^{-4} s^{-1}$ and $\sim 10^{3} s^{-1}$ strain rate effects have negligible influence on ultimate strain. Quasi-static values of ultimate strain may be used confidently at these strain rates.

At strain rates above $10^{3} s^{-1}$, flow stress is apparently increased, resulting in a more even distribution of strains. As a result, the strain does not concentrate into a single necked region, but instead involves the bulk of the material in the specimen. As discussed in Section 4, the increase in ultimate strain may be attributed to strain and strain-rate hardening, and to the effects of applied triaxial stresses. As shown by Bridgeman,[20] a nearly hydrostatic stress state will allow uniform straining to relatively high ultimate strains.

We recommend further testing with the exploding cylinder technique discussed in this paper. This testing should be done and the results should be compared to split Hopkinson bar measurements. As a result of this testing, the effects of strain rate and stress state on ultimate strain will be more clearly delineated. Continued testing with Electrolytic Tough Pitch copper would provide a broader data base from which the premises presented in this paper could be studied. Extension to other materials would also be a natural step. With existing methods,

the exploding cylinder technique may be used to determine material behavior to strain rates greater than $3 \times 10^4 s^{-1}$.

REFERENCES

1. Manjoine, M. J., "Influence of Rate of Strain and Temperature on Yield Stresses of Mild Steel", J. App. Mech., 11, Trans. ASME, 66, 1944.

2. Nicholas, T., "Mechanical Properties of Structural Grades of Beryllium at High Strain Rates", AFML-TR-75-168, ADA 020-076, October 1975.

3. Hancock, J. W. and Mackenzie, A. C. "On the Mechanisms of Ductile Failure in High Strength Steels Subjected to Multiaxial Stress-States", J. Mech. Phys. Solids, 24, 1976.

4. Bitans, K. and Whitton, P. W., "Stress-Strain Curves for Oxygen-Free High Conductivity Copper at Shear Strain Rates Up to $10^3 s^{-1}$", Proc. Inst. Mech. Engr., 1970-71.

5. Duffy, J., Hawley, R. H. and Frantz, R. A., "The Deformation of Lead in Torsion at High Strain Rates", J. Appl. Mech., 38, 1971.

6. Isozaki, T., Ohba, T. and Veda, S., "High Velocity Tensile Tests of Austenite Stainless Steel at Elevated Temperatures", Bull. ASME 20, 278-284, 1977.

7. Schultz, A. B., Tuschak, P. A., and Vicario, Jr., A. A., "Experimental Evaluation of Material Behavior in a Wire Under Transverse Impact, J. of Appl. Mech., Volume 34, No. 2, Trans. ASME, Volume 89, Series E, pp 392-396, June 1967.

8. Schultz, A. B., "Dynamic Behavior of Metals Under Tensile Impact, Part 1, Elevated Temperature Tests", AFML-TR-69-76, AD8-53-260, April 1969.

9. Hoggatt, C. R. and Recht, R. F., "Experimental Determinations of Dynamic Stress-Strain Relationships," Center for High Energy Forming, Denver, Colorado, August 1968.

10. Metals Handbook, American Society for Metals, Vol. 1, 8th Edition, 1961.

11. Leopold, H. S., Effect of Bridgewire Parameters on Explosive Initiation in Exploding Wires, Vol. 3, Ed. by Chase and Moore, Plenum Press, 1964.

12. Kury, J. W., Hornig, H. C., Lee, E. L., McDonel, J. L., Ornellas, D. L., Finger, M., Strange, F. M., and Wilkins, M. L., "Metal Acceleration by Chemical Explosive," Fourth International Symposium on Detonation, AD 656035, pp 3-11, 1966.

13. Preonas, D. D., and Prater, R. F., "Quantitative Motion Analysis from Rotating Mirror Framing Camera Records," J. of the SMPTE, Vol. 79, July 1970.

14. Osborn, J., "Explosive Expansion of Copper Cylinders," Memo for Record, 22 April 1977.

15. Zener, C., "Fracturing of Metals", ASM 3, 1948.

16. Recht, "Catastrophic Thermoplastic Shear", J. App. Mech., June 1964.

17. Backofen, W. A., Deformation Processing, Addison Wesley, Chapter 12, 1972.

18. Low, J. R., Jr., "Behavior of Metals Under Direct Non-reversed Loading", Properties of Metals in Materials Engineering, Am. Soc. Met., pp 35, 1949.

19. Taylor, G. I., Scientific Papers of G. I. Taylor, Cambridge University Press, Cambridge, England 1963, Vol. III.

20. Hoggatt, C. R., and Recht, R. F., "Fracture Behavior of Tubular Bombs", J. App. Phys., 39, Feb. 1968.

21. Famiglietti, M., U. S. Army Ballistics Research Laboratory, Memo Report No. 597, March 1952.

22. Allison, F. E. and Schrienpf, J. T., J. Appl. Phys., 31, p 846, 1960.

23. Kumar, A., and Kumble, R. G., "Viscous Drag and Dislocations at High Strain Rates in Copper", J. App. Phys., Vol. 40, August 1969.

24. Bridgeman, P. W., Studies in Large Plastic Flow and Fracture, McGraw-Hill, 1st Ed., 1952, Chapter 4.

25. Eleiche, A. M., and Campbell, J. D., "The Influence of Strain-Rate History on the Shear Strength of Copper and Titanium at Large Strains", University of Oxford Report No. 1106/74, October 1974.

APPENDIX

FRAMING CAMERA RECORDS AND STRAIN VERSUS TIME PLOTS FOR UDRI EXPLODING CYLINDERS

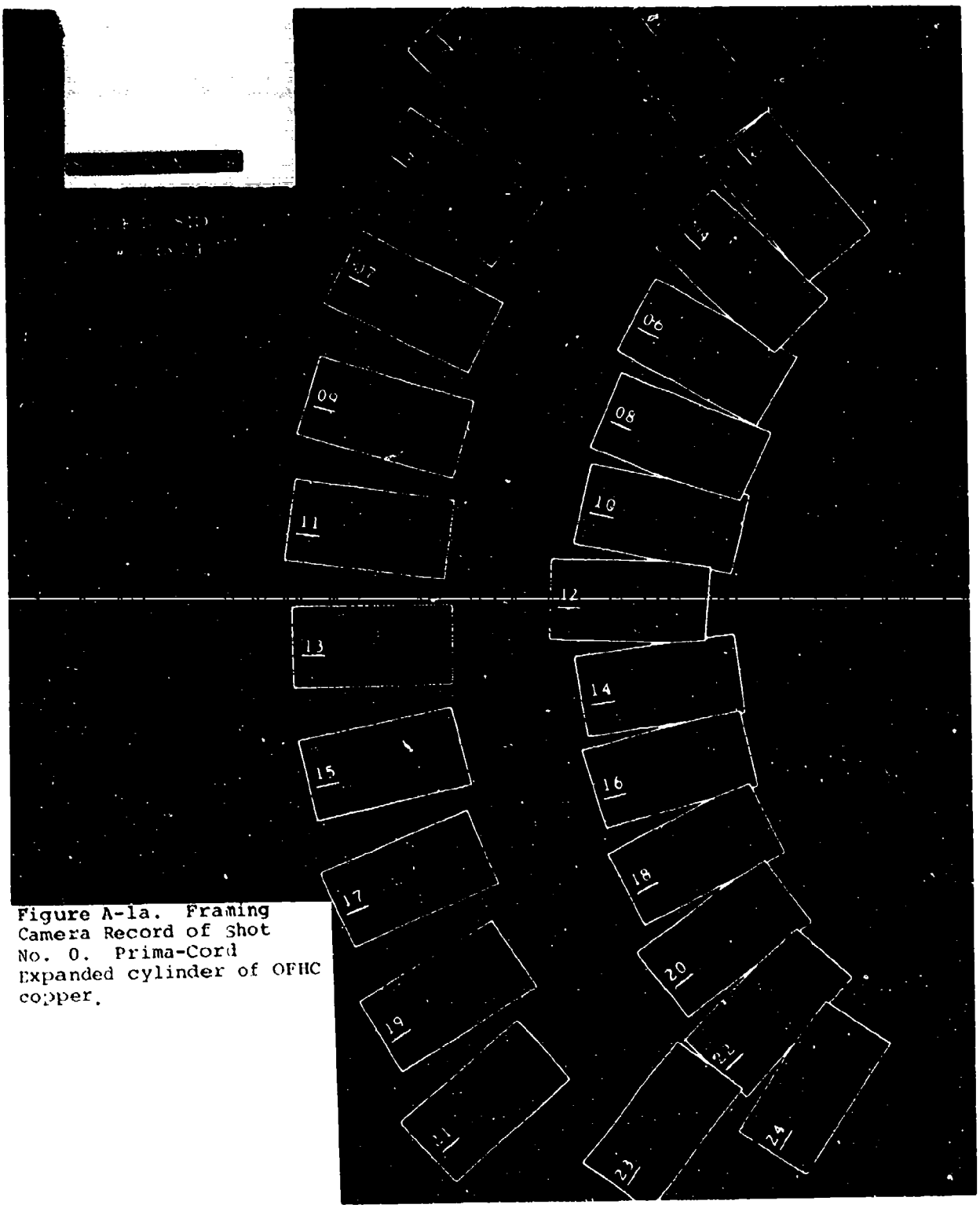

Figure A-1a. Framing Camera Record of Shot No. 0. Prima-Cord Expanded cylinder of OFHC copper.

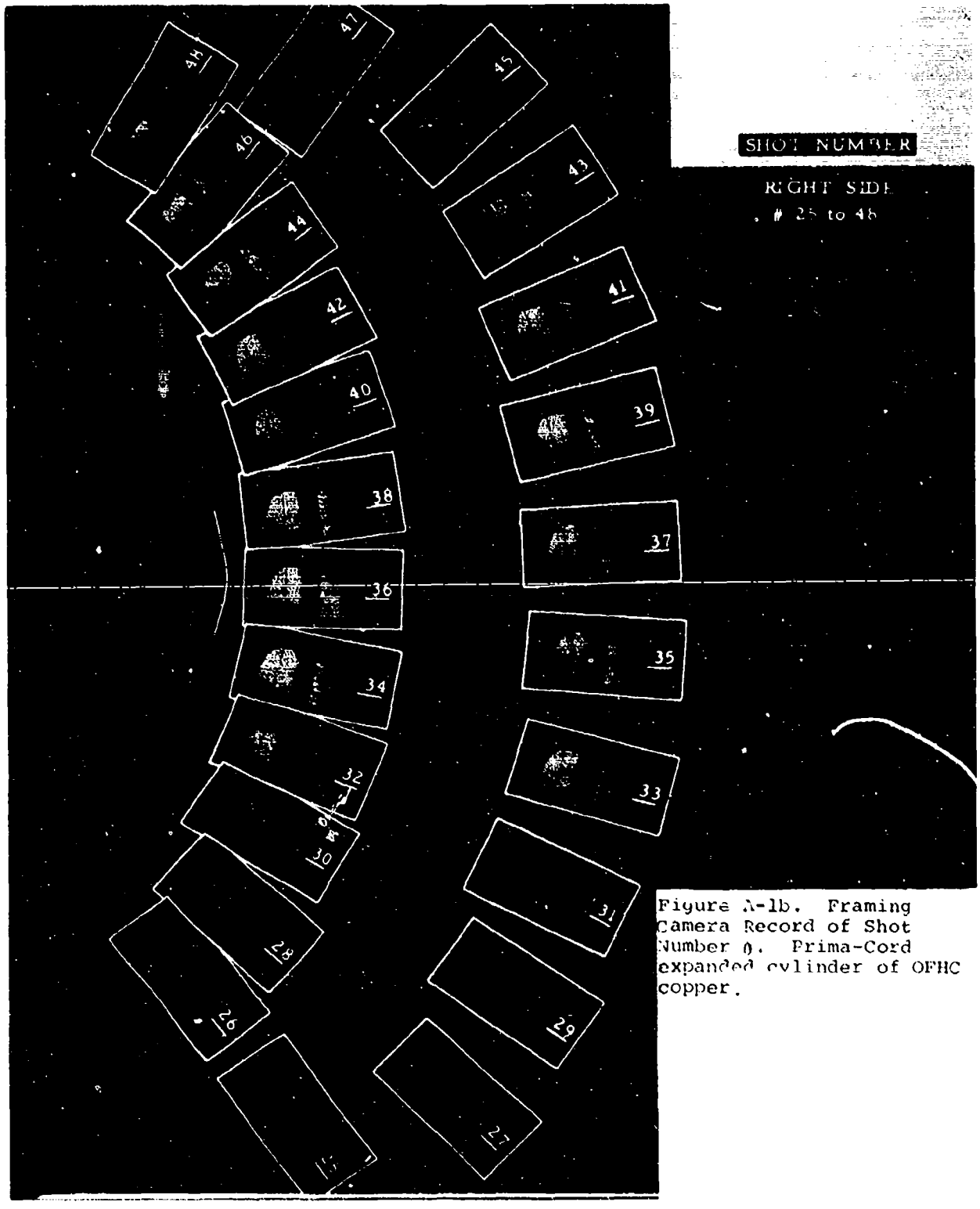

Figure A-1b. Framing Camera Record of Shot Number 0. Prima-Cord expanded cylinder of OFHC copper.

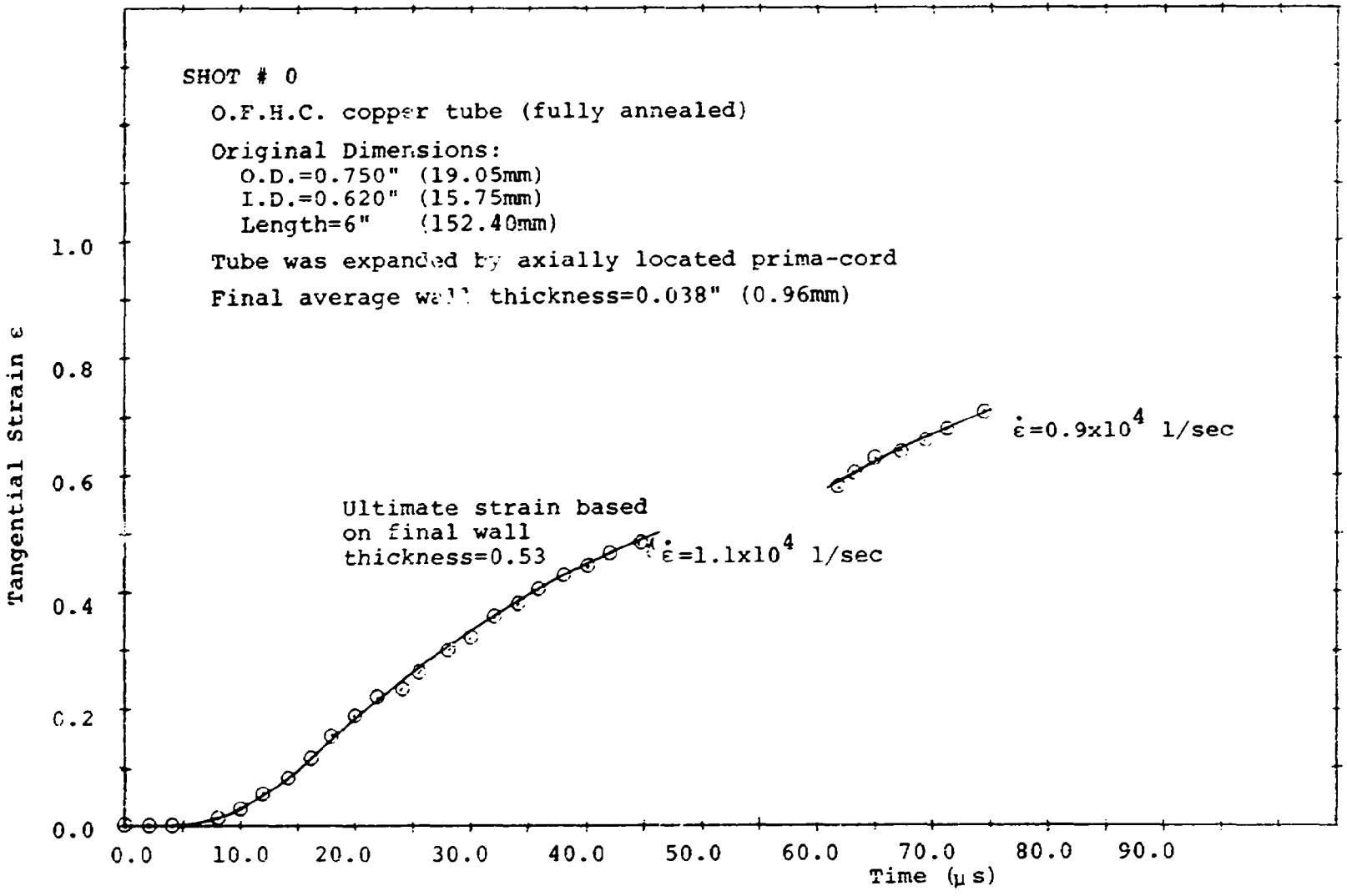

Figure A-2. Strain Versus Time for Copper Tube Expanded by Prima-Cord

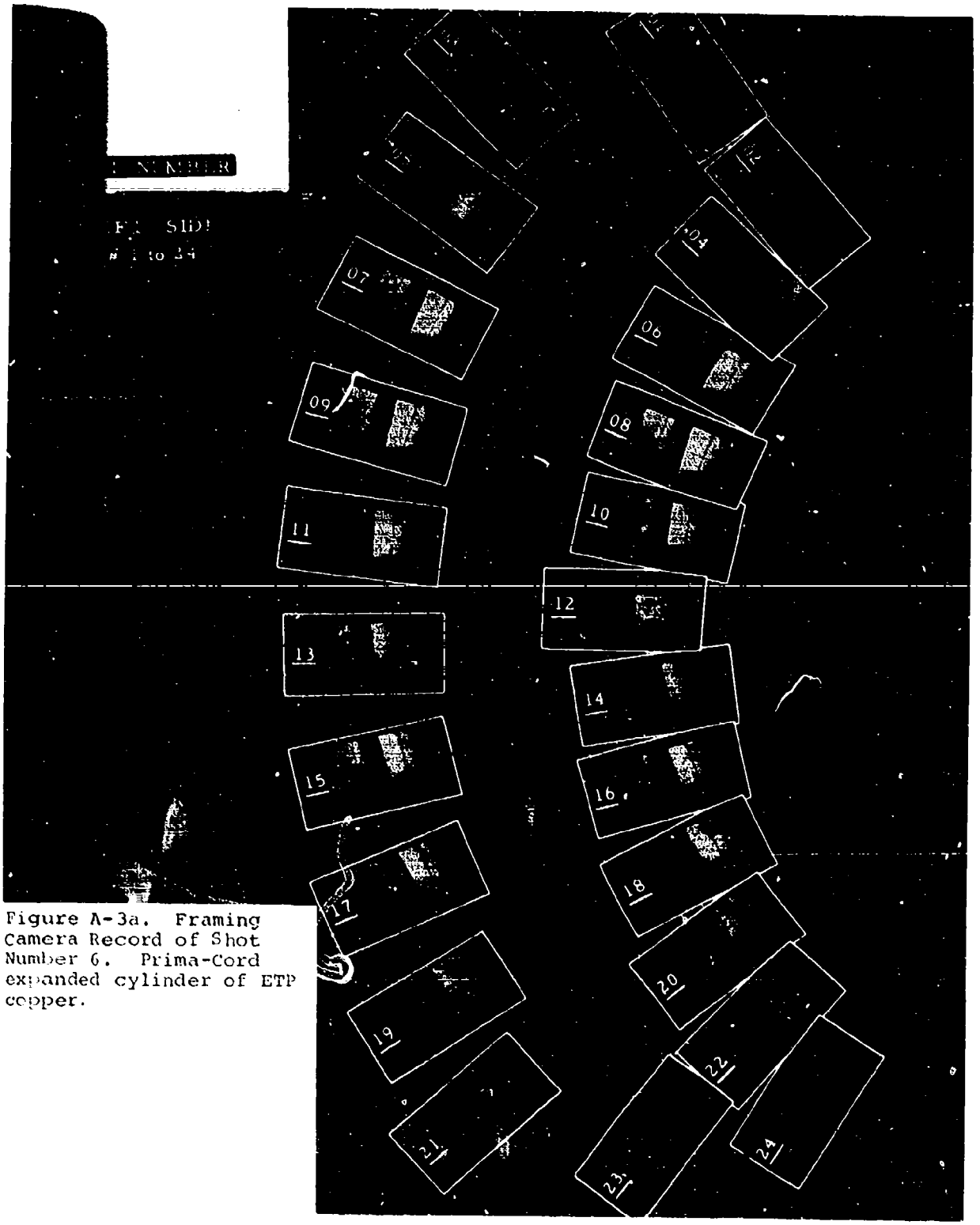

Figure A-3a. Framing Camera Record of Shot Number 6. Prima-Cord expanded cylinder of ETP copper.

Figure A-3b. Framing Camera Record of Shot Number 6. Prima-Cord expanded cylinder of OFP copper.

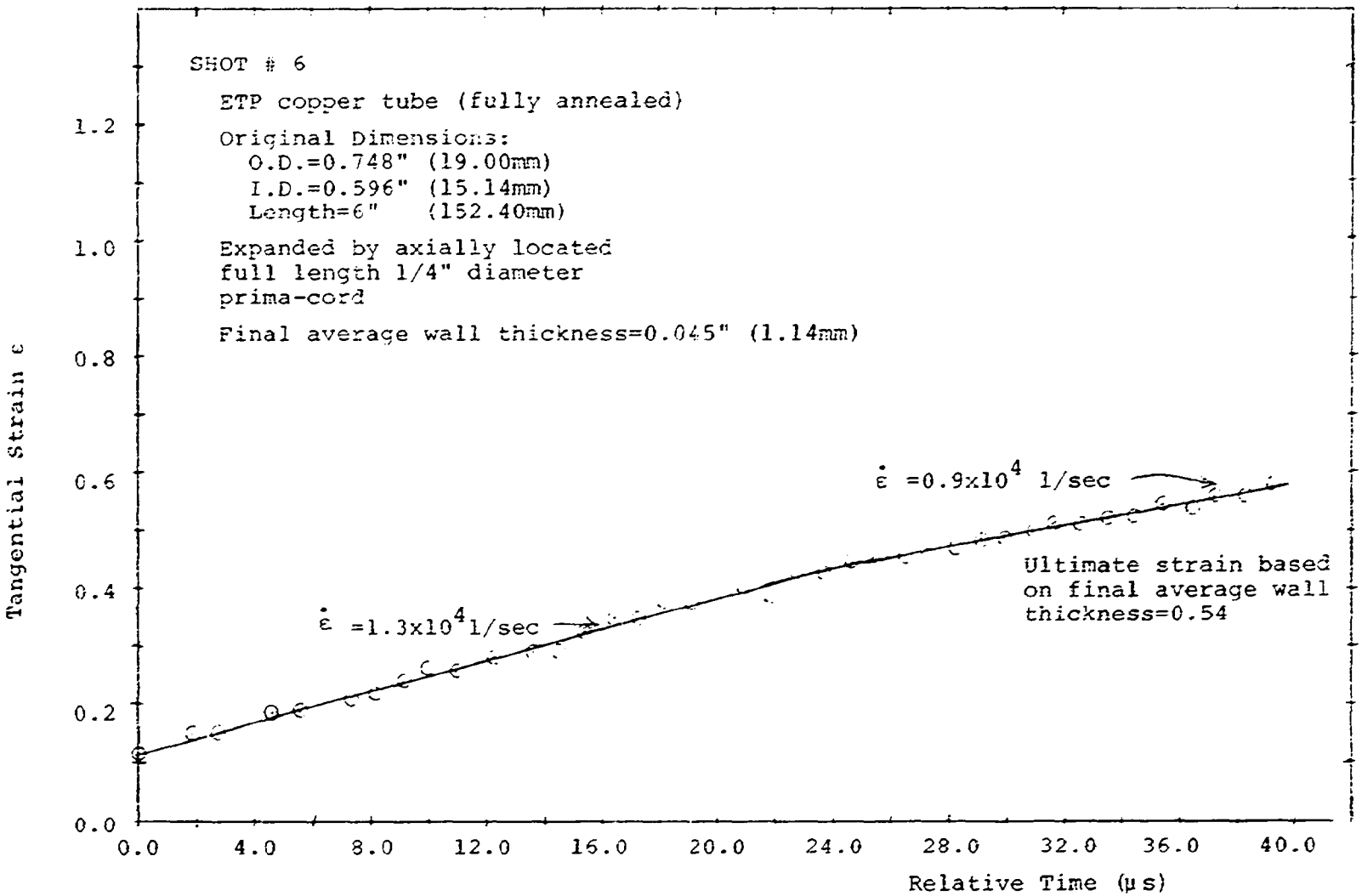

Figure A-4. Strain Versus Time for Prima-Cord Expanded Copper Tube. Time equal to zero is first readable frame on film.

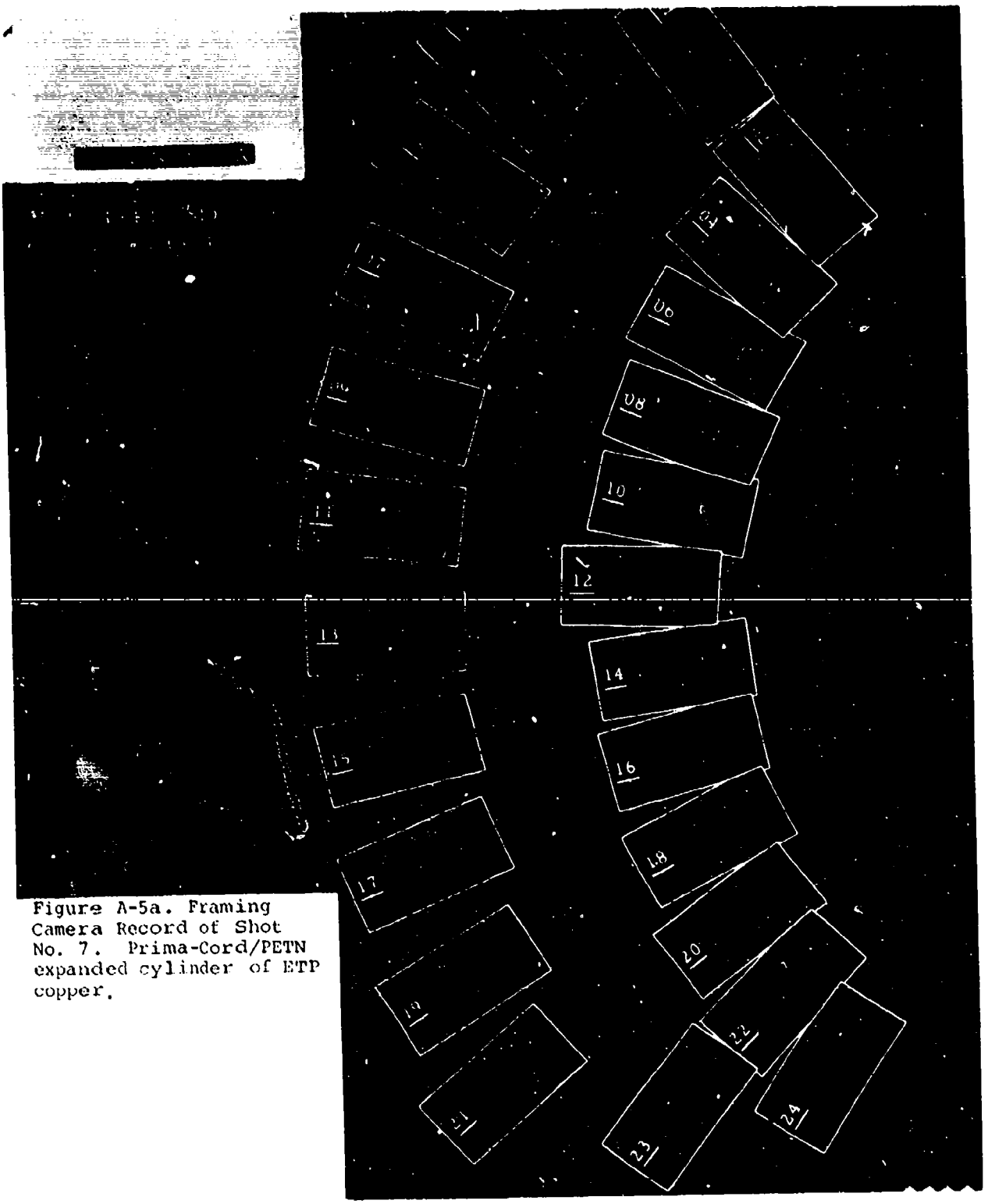

Figure A-5a. Framing Camera Record of Shot No. 7. Prima-Cord/PETN expanded cylinder of ETP copper.

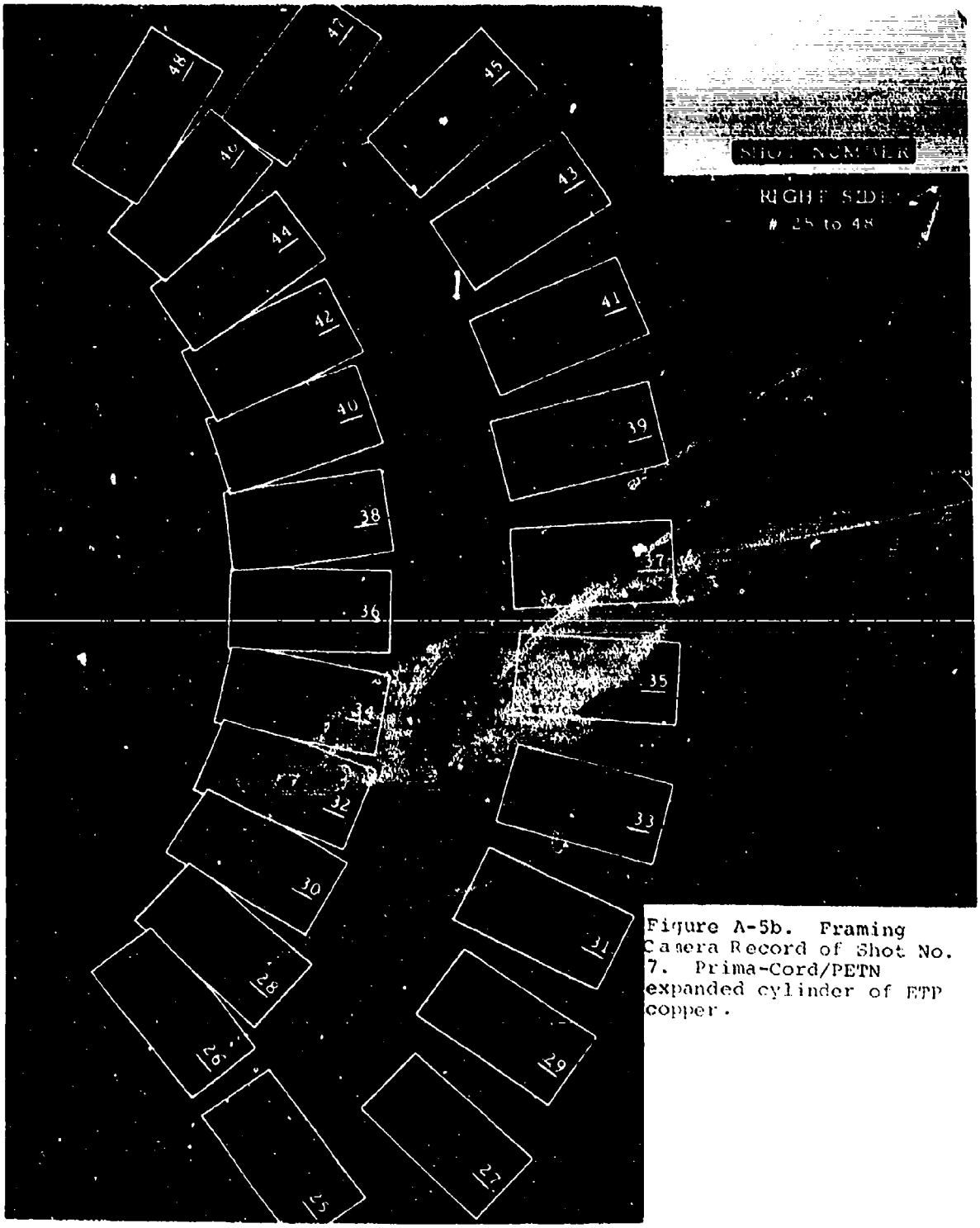

Figure A-5b. Framing Camera Record of Shot No. 7. Prima-Cord/PETN expanded cylinder of ETP copper.

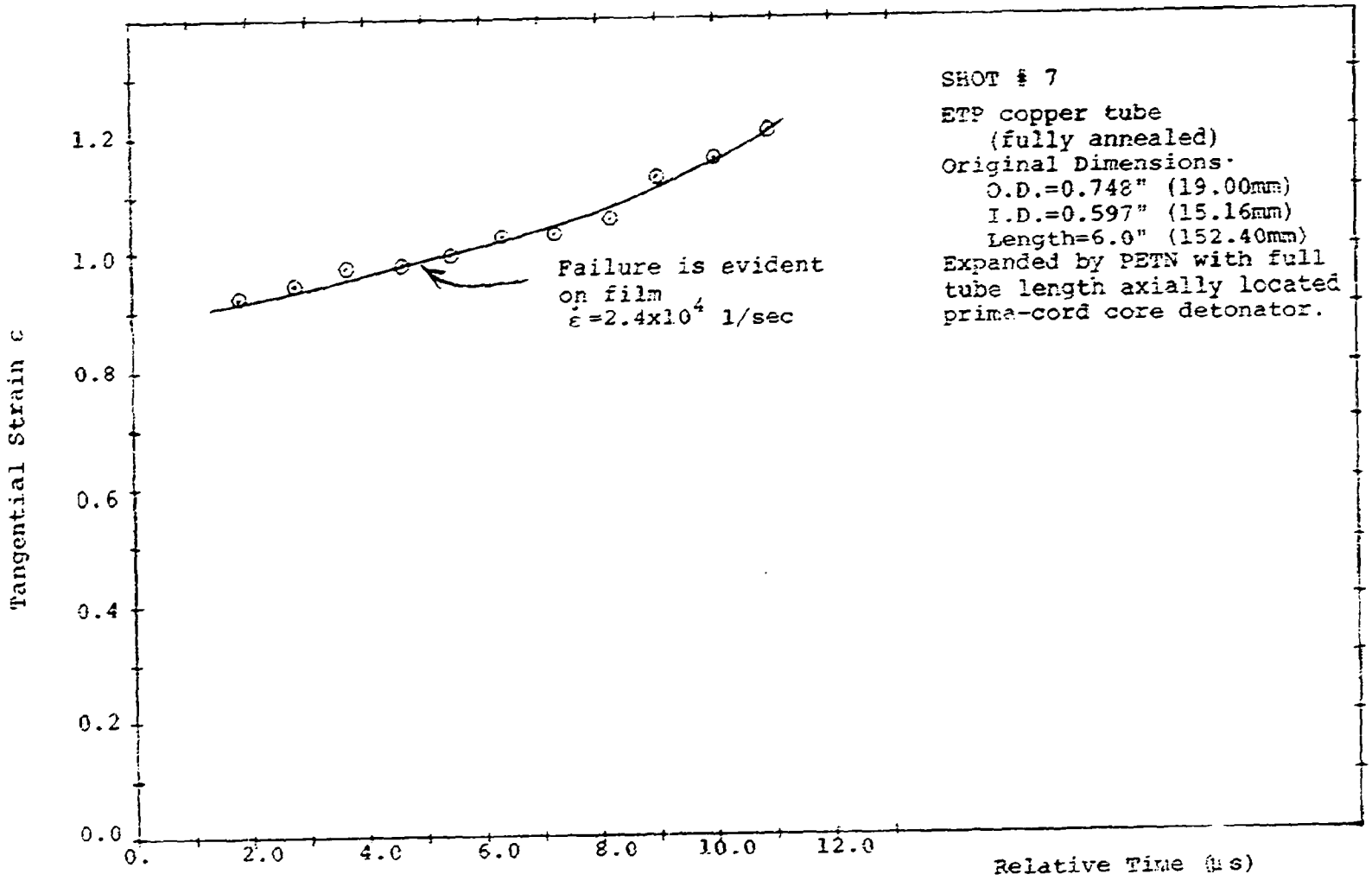

Figure A-6. Strain Versus Time for ETP Copper Tube.
Time equal to zero is first readable frame of film.

Figure A-7a. Framing Camera Record of Shot Number 16. Explosively formed projectile (EFP) with explosive charge and explosive bridge wire (EBW) detonator. LTP copper cylinder.

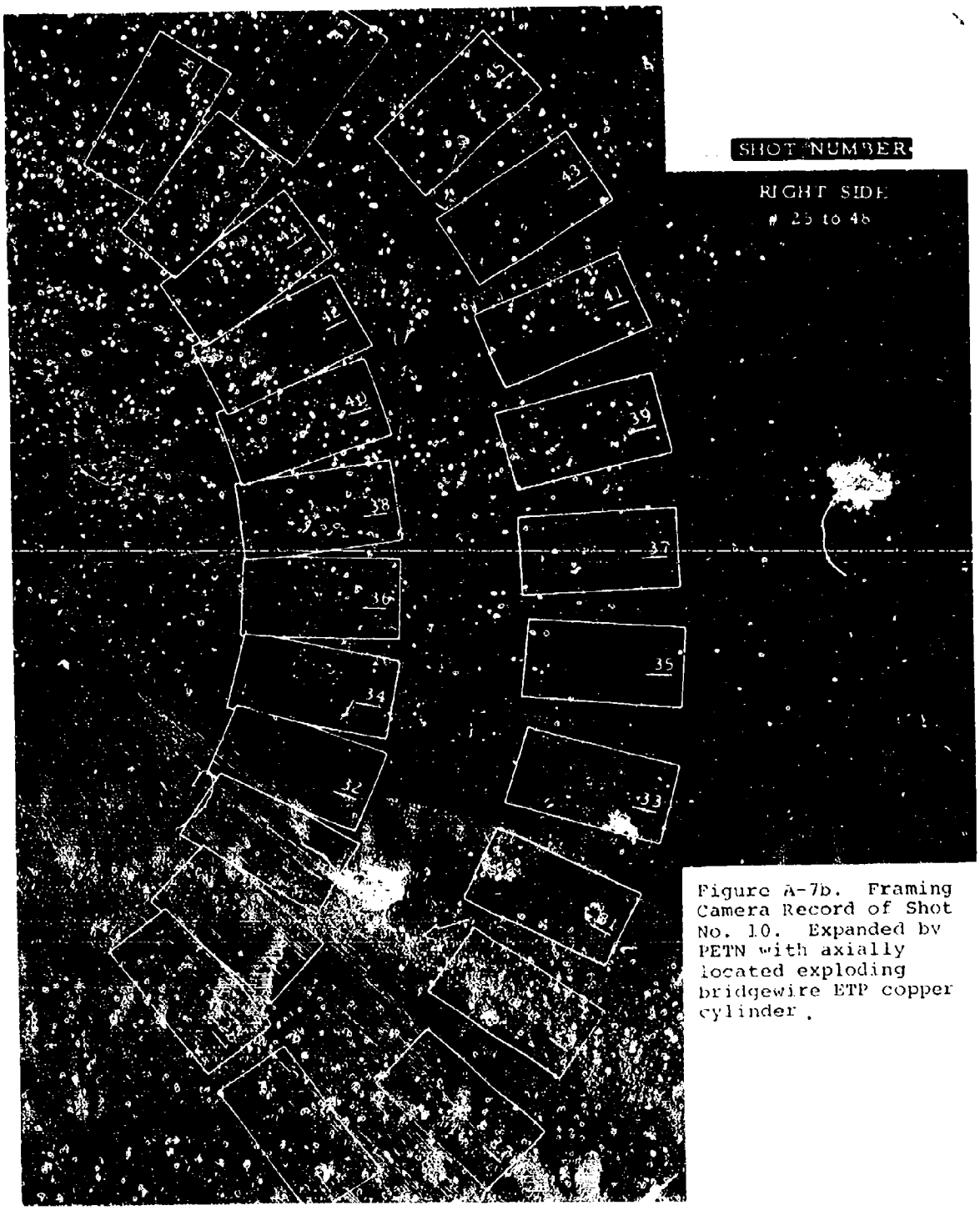

Figure A-7b. Framing Camera Record of Shot No. 10. Expanded by PETN with axially located exploding bridgewire ETP copper cylinder.

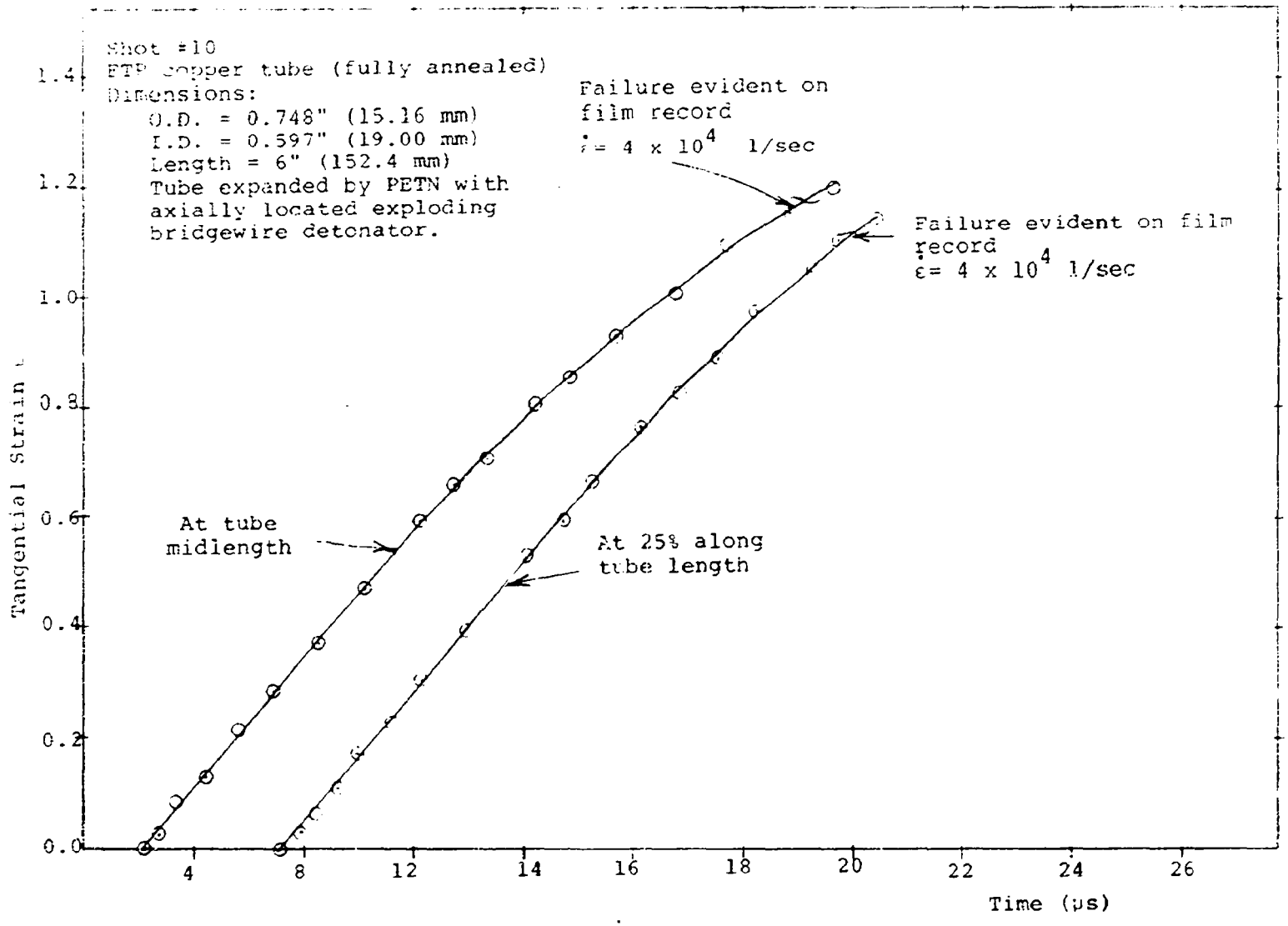

Figure A-8. Strain Versus Time for Copper Tube Expanded by PETN